Supplementary Information for:

A General Flame Aerosol Route to Kinetically Stabilized Metal-Organic Frameworks

Shuo Liu[1,2], Chaochao Dun[2,*], Feipeng Yang[3], Kang-Lan Tung[1], Dominik Wierzbicki[3,4], Sanjit Ghose[3], Kaiwen Chen[1], Linfeng Chen[2], Richard Ciora[1], Mohd A. Khan[1], Zhengxi Xuan[1,5], Miao Yu[1,5], Jeffrey J. Urban[2,*], and Mark T. Swihart[1,5,*]

[1] Department of Chemical and Biological Engineering, University at Buffalo, The State University of New York, Buffalo, NY 14260, USA

[2] The Molecular Foundry, Lawrence Berkeley National Laboratory, Berkeley, CA 94720, USA

[3] National Synchrotron Light Source Ⅱ, Brookhaven National Laboratory, Upton, NY 11973, USA

[4] AGH University of Science and Technology, Faculty of Energy and Fuels, Al. A. Mickiewicza 30, 30-059 Cracow, Poland

[5] RENEW Institute, University at Buffalo, The State University of New York, Buffalo, NY 14260, USA

Supplementary Figures

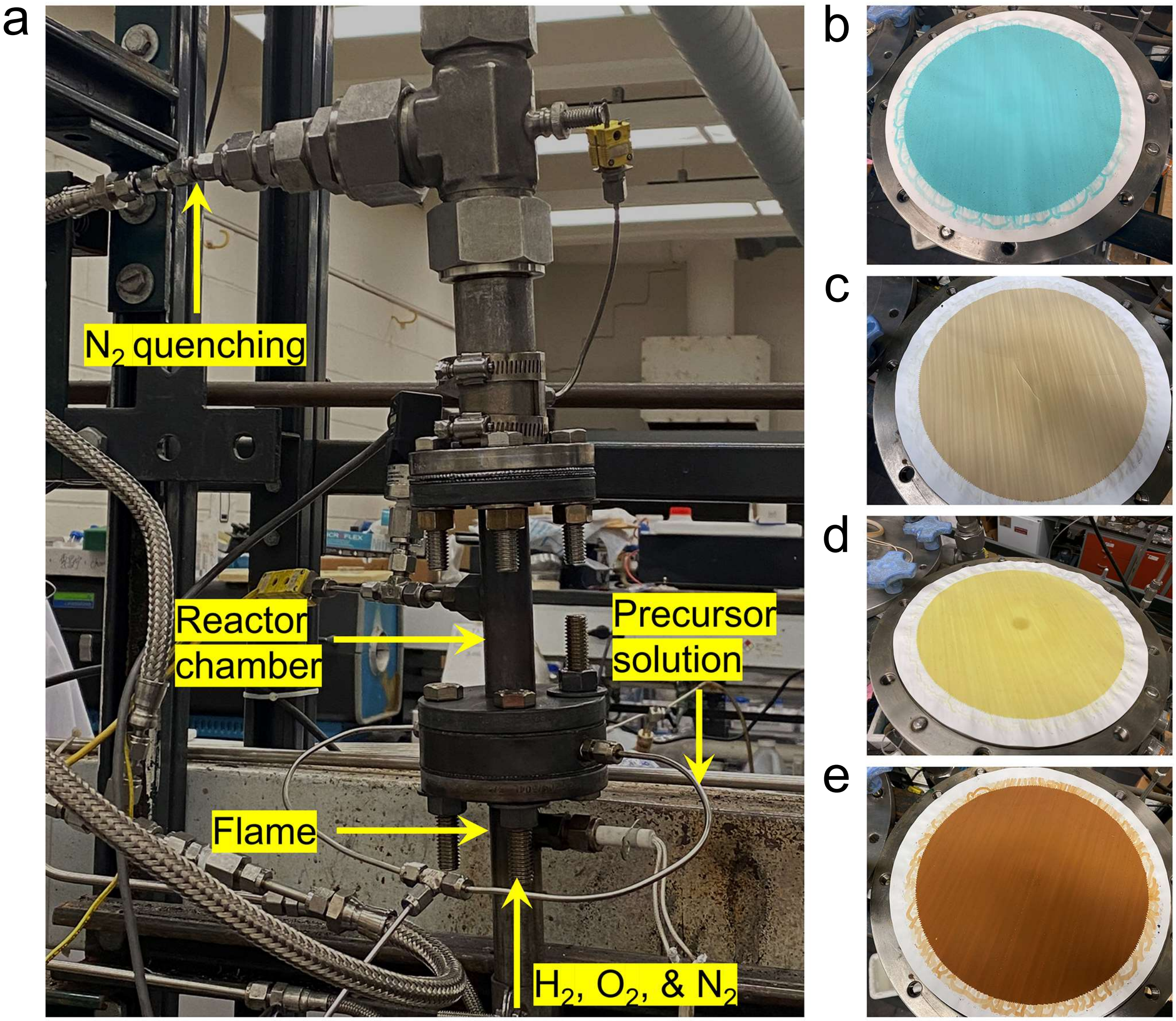

Supplementary Fig. 1. Photographs of **a.** the flame reactor in operation, and the produced **b.** Cu HKUST-1, **c.** Zn BDC-NH2, **d.** amorphous Zr UiO-66-NH2, and **e.** amorphous Fe FMA collected on filter membranes. The diameter of filter membrane is 29.3 cm. The production yield of MOFs is 0.3~1 g/h in the current laboratory-scale reactor.

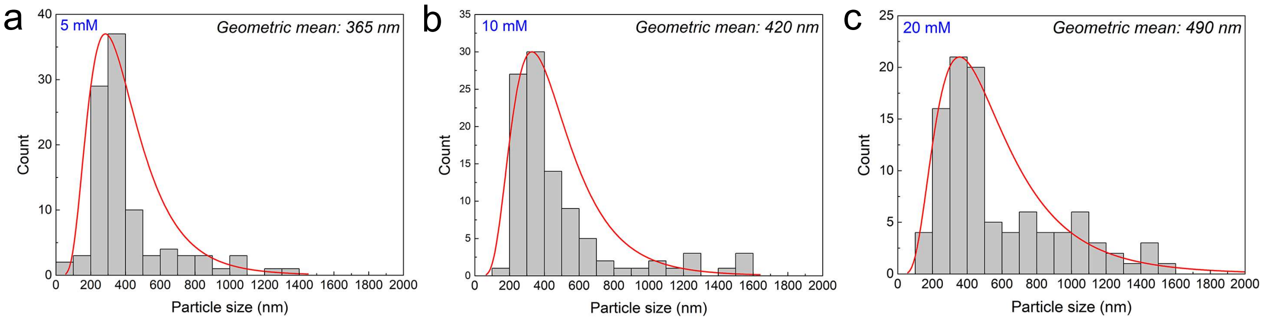

Supplementary Fig. 2. Particle size distribution of crystalline Cu HKUST-1 MOFs synthesized by **a.** 5 mM, **b.** 10 mM, and **c.** 20 mM Cu ion precursors, based on statistics of 100 particles in SEM images. The particle size distribution was analyzed using ImageJ software.

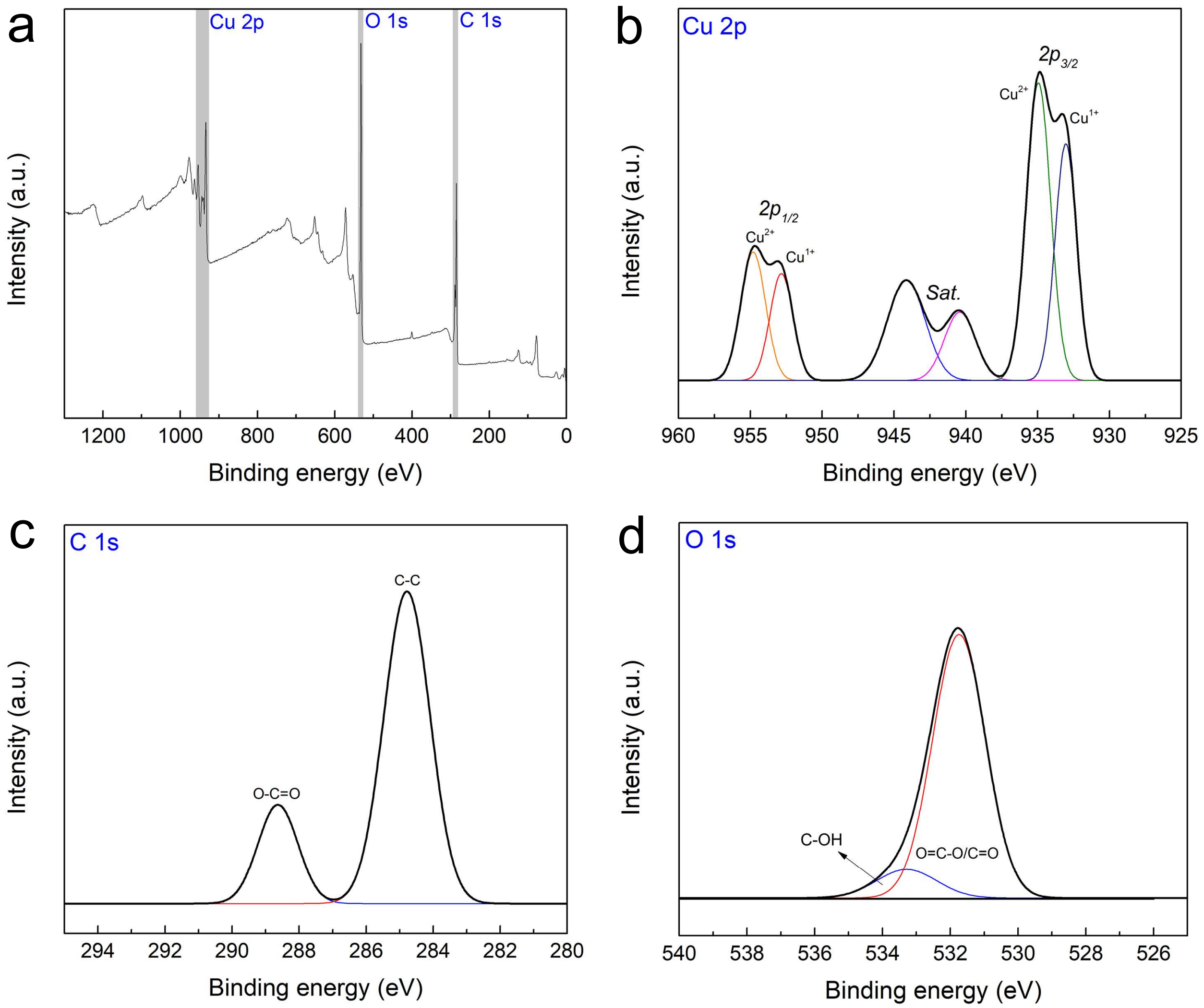

Supplementary Fig. 3. XPS spectrum of flame synthesized Cu HKUST-1. **a.** Survey spectrum; **b.** Cu *2p*; **c.** C 1s; and **d.** O 1s energy ranges.

Cu, C, and O were detected in the flame synthesized Cu HKUST-1. The Cu ions existed as Cu^{2+} and Cu^{+} on the sample surface; the C *1s* spectrum mainly showed C–C sp^2 bonds, as well as a peak for O-C=O bonds from the carboxyl group of Cu HKUST-1; the O *1s* spectrum showed the main bonds for C=O/O-C=O by carboxyl groups and its split peak for C–OH bonds. This XPS spectrum was consistent with previously reported Cu HKUST-1 MOFs.[1]

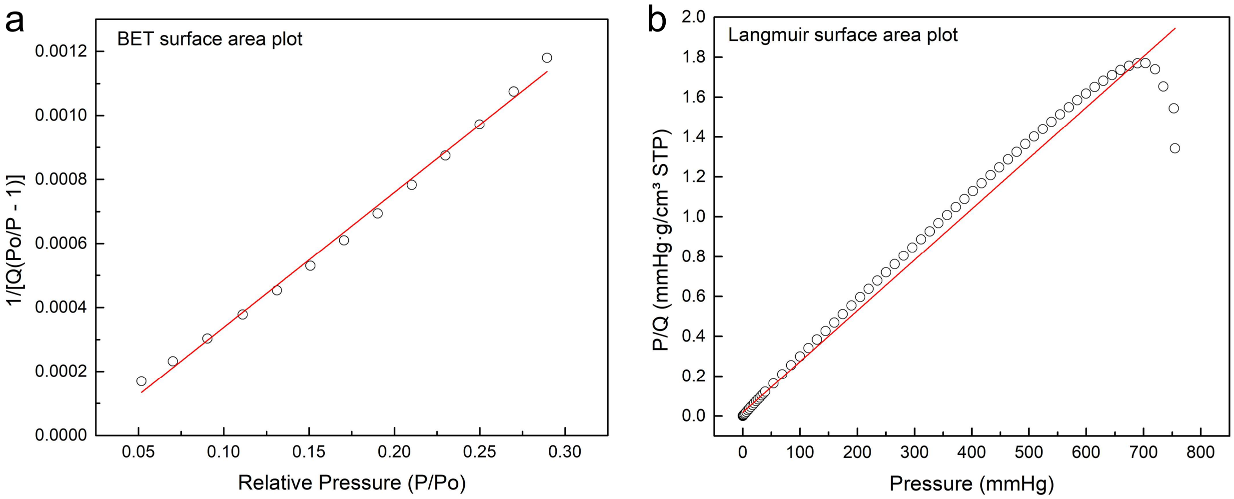

Supplementary Fig. 4. Plots utilized to determine the **a.** BET and **b.** Langmuir surface area of the flame synthesized Cu HKUST-1 shown in Fig. 3e.

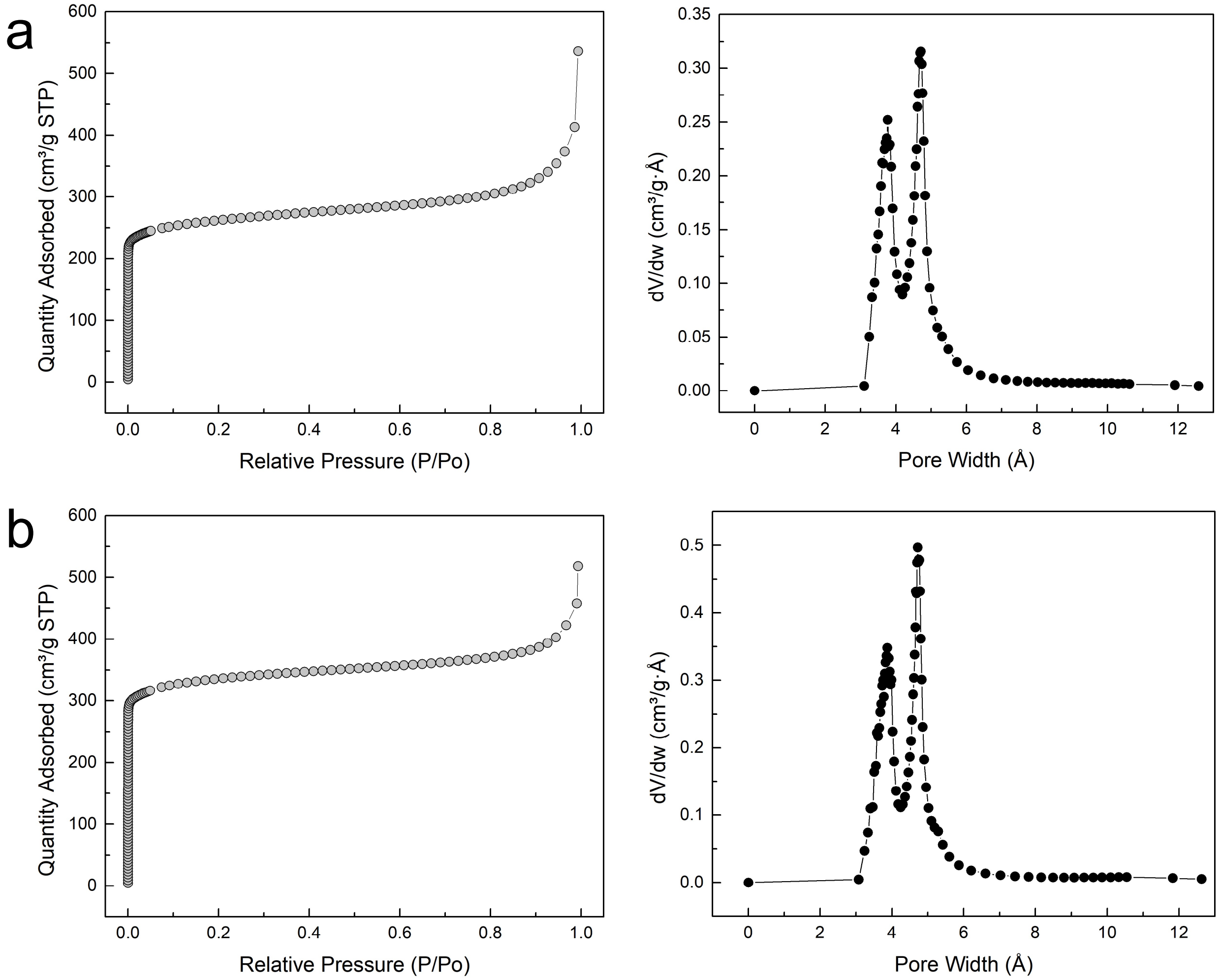

Supplementary Fig. 5. N_2 adsorption isotherm plots and Horvath-Kawazoe differential pore volume plots of Cu HKUST-1 prepared using **a.** 20 mM and **b.** 40 mM Cu^{2+} concentrations, as shown in Supplementary Table 3.

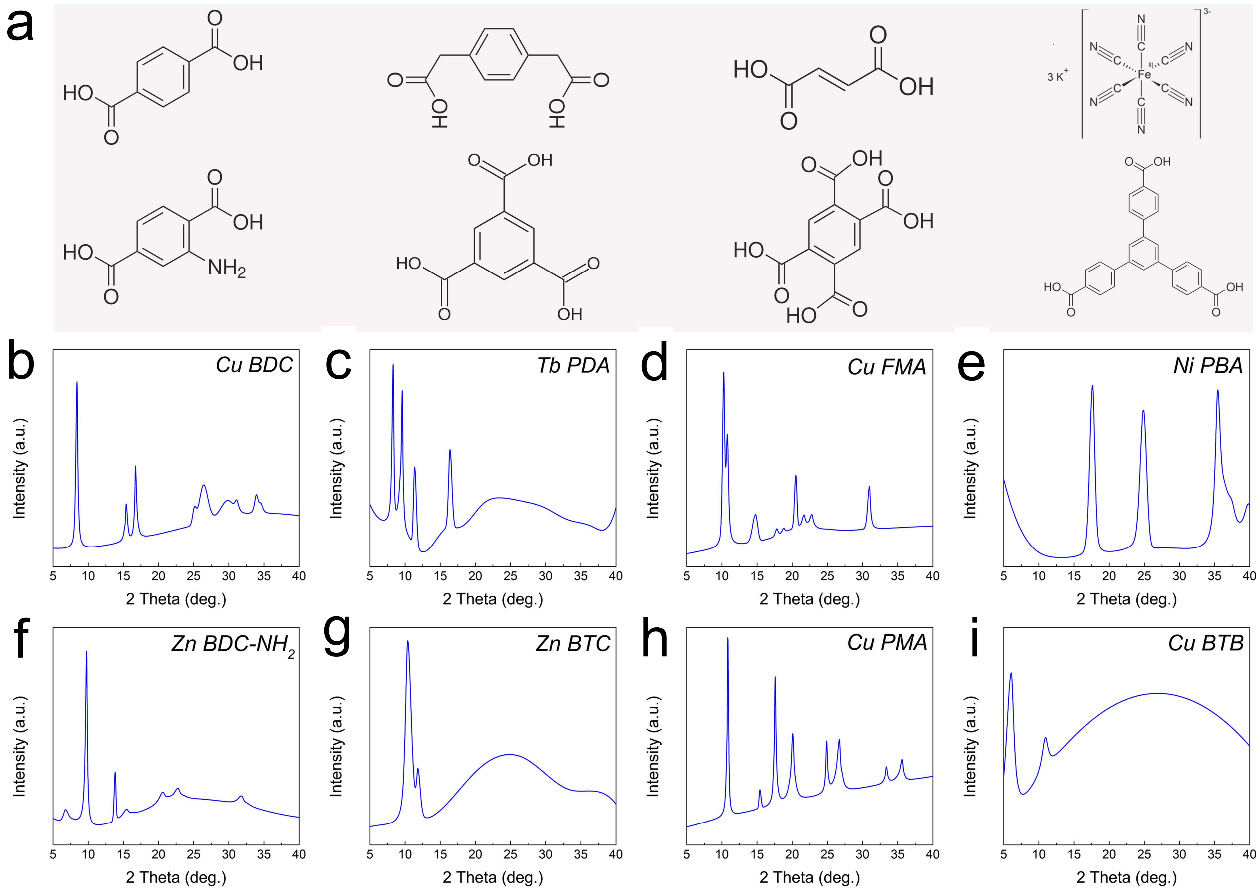

Supplementary Fig. 6. Library of flame aerosol synthesized crystalline MOFs. **a.** Chemical structures of 1,4-BDC, 1,4-PDA, fumaric acid, potassium ferricyanide, 1,4-BDC-NH_2, 1,3,5-BTC, pyromellitic acid, and 1,3,5-BTB; Rietveld refined XRD patterns of **b.** Cu BDC; **c.** Tb PDA; **d.** Cu FMA; **e.** Ni PBA; **f.** Zn BDC-NH_2; **g.** Zn BTC; **h.** Cu PMA; and **i.** Cu BTB. Detailed peak information is provided in Supplementary Table 5-12.

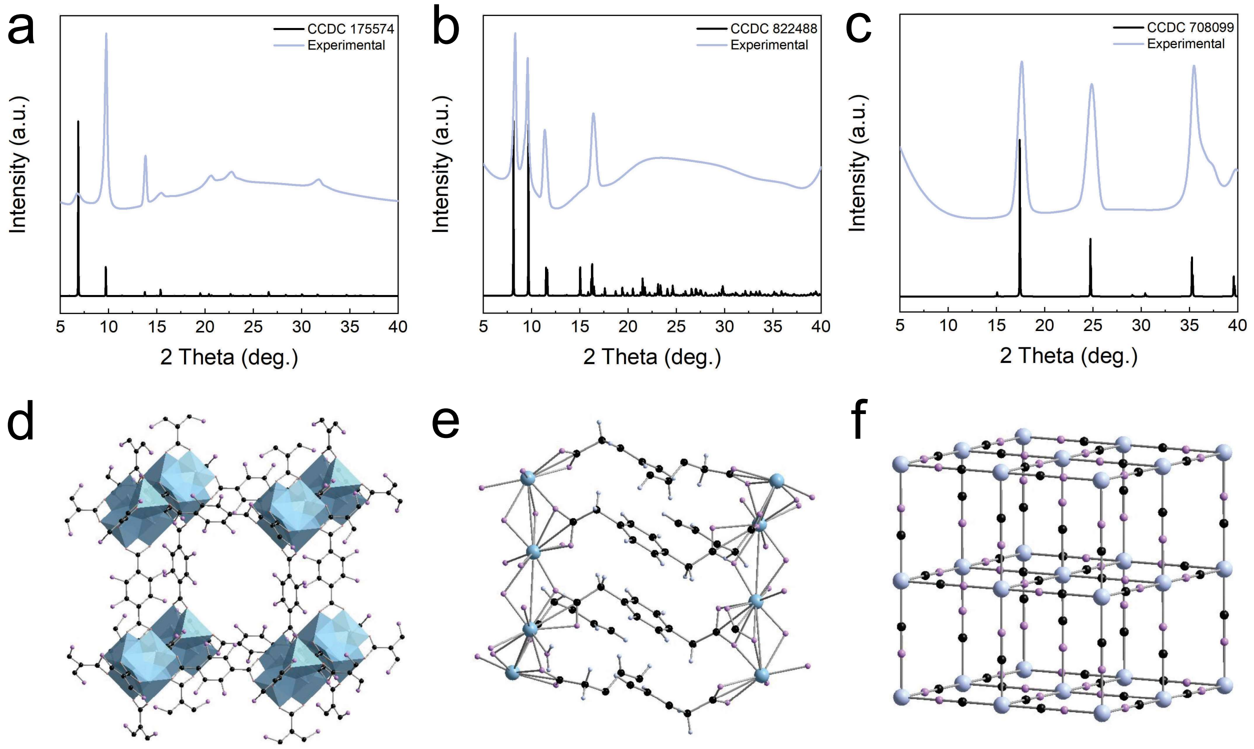

Supplementary Fig. 7. MOFs structure of the as-synthesized **a, d.** Zn BDC-NH_2, **b, e.** Tb PDA, and **c, f.** Ni PBA.

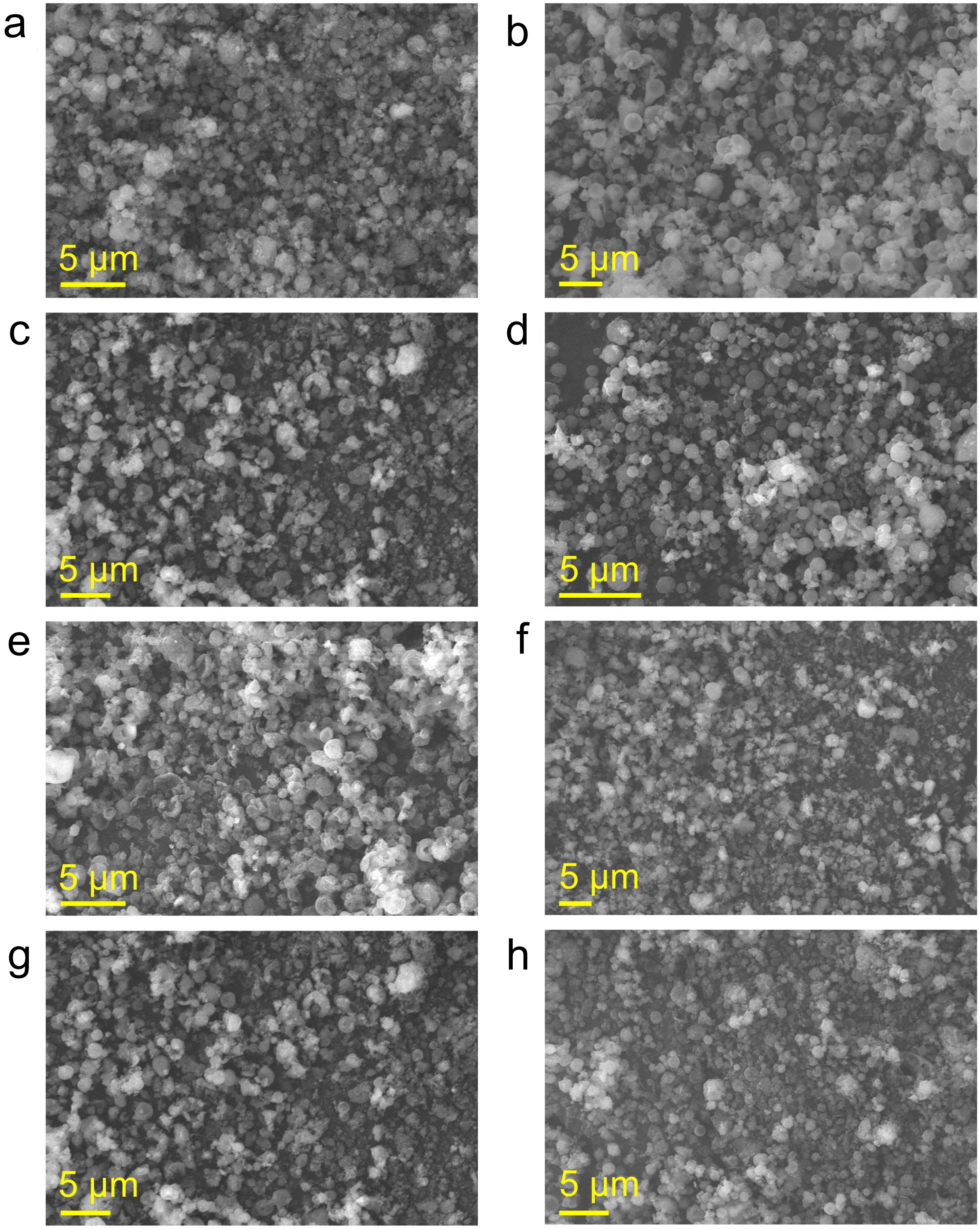

Supplementary Fig. 8. Representative SEM images of flame synthesized crystalline MOFs. **a.** Cu BDC; **b.** Tb PDA; **c.** Cu FMA; **d.** Ni PBA; **e.** Zn BDC-NH_2; **f.** Zn BTC; **g.** Cu PMA; and **h.** Cu BTB.

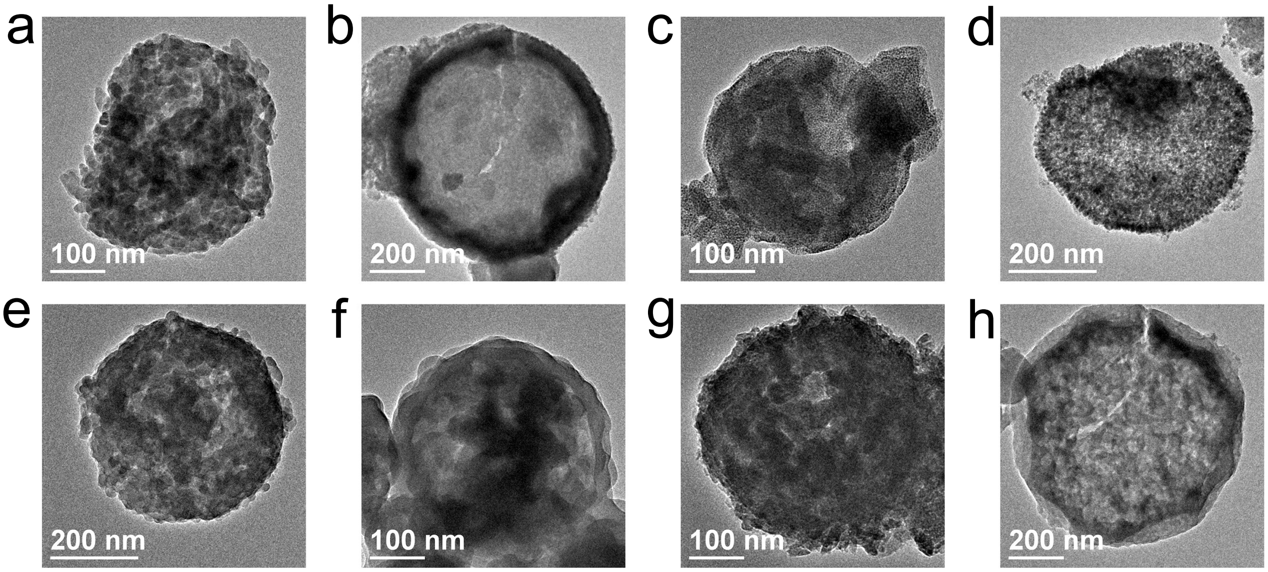

Supplementary Fig. 9. Representative TEM images of flame synthesized crystalline MOFs. **a.** Cu BDC; **b.** Tb PDA; **c.** Cu FMA; **d.** Ni PBA; **e.** Zn BDC-NH_2; **f.** Zn BTC; **g.** Cu PMA; and **h.** Cu BTB.

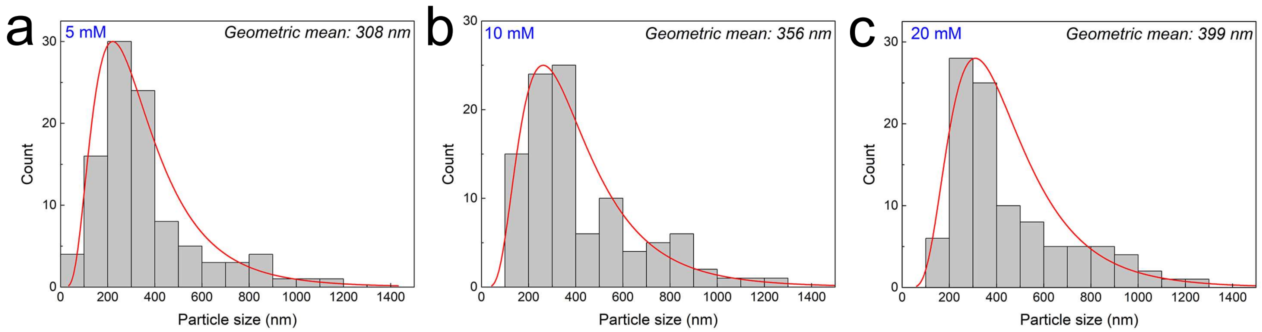

Supplementary Fig. 10. Particle size distribution of amorphous Zr FMA MOFs synthesized using **a.** 5 mM, **b.** 10 mM, and **c.** 20 mM Zr ion precursors, based on statistics of 100 particles in SEM images. The particle size distribution was analyzed using ImageJ software.

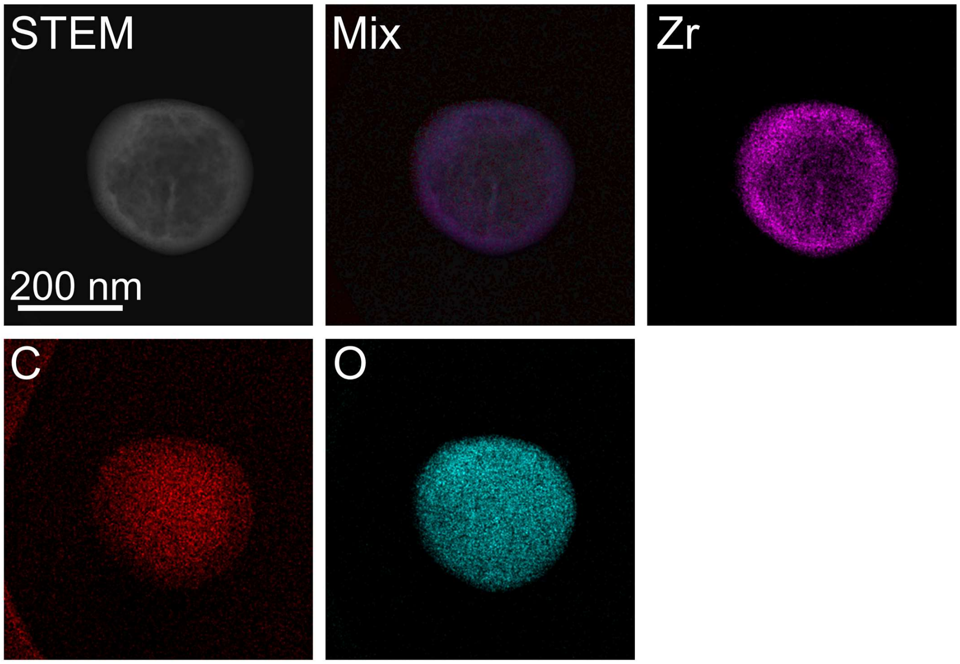

Supplementary Fig. 11. HAADF-STEM elemental maps of amorphous Zr FMA MOF.

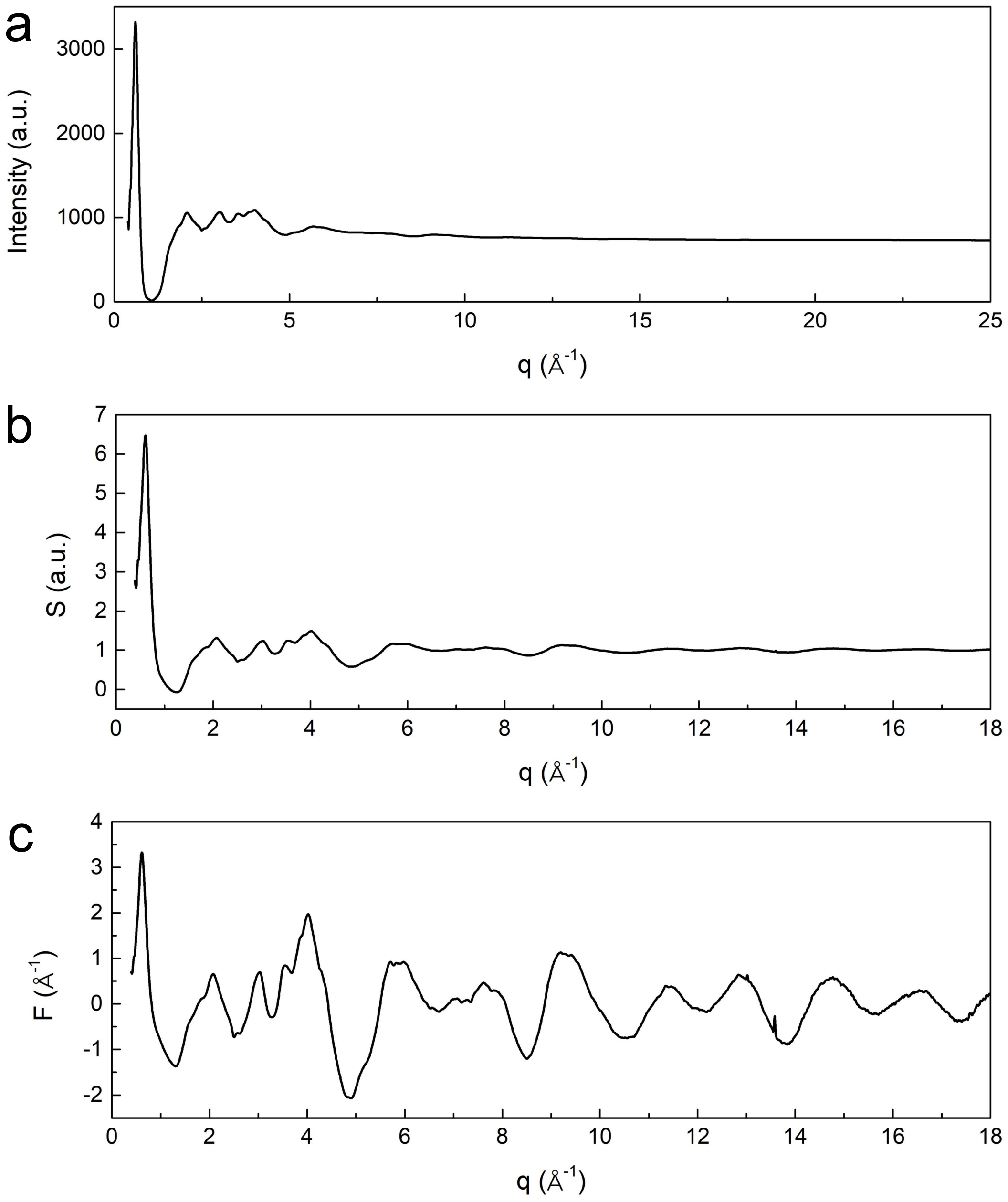

Supplementary Fig. 12. a. X-ray total scattering pattern; **b.** Static structure factor S(Q); and **c.** Fourier transform function of S (Q) for the amorphous Zr FMA MOF corresponding to Fig. 4c.

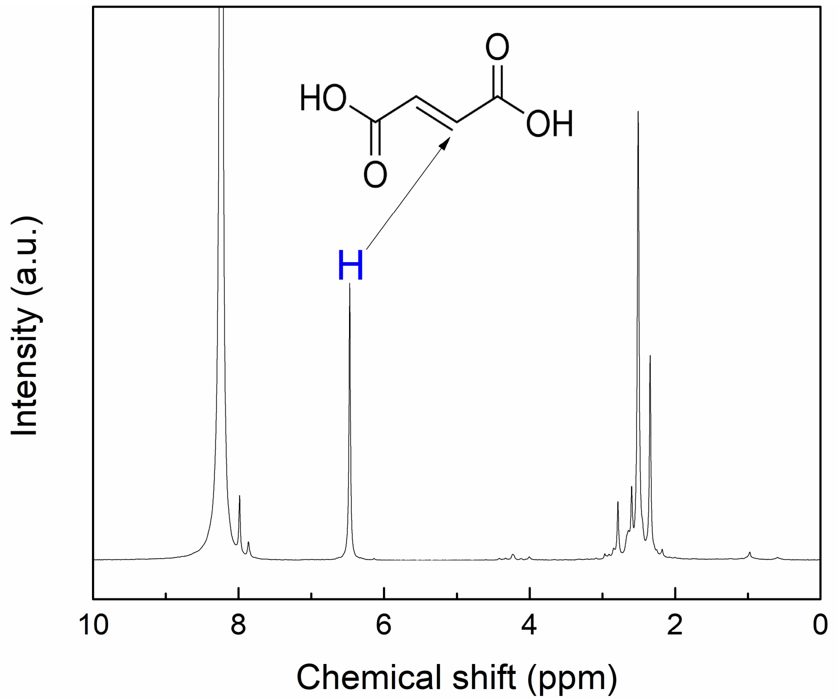

Supplementary Fig. 13. ^{1}H NMR spectrum of amorphous Zr FMA. The MOF was digested in a mixture of 35% DCl in D_2O and DMSO-d6.

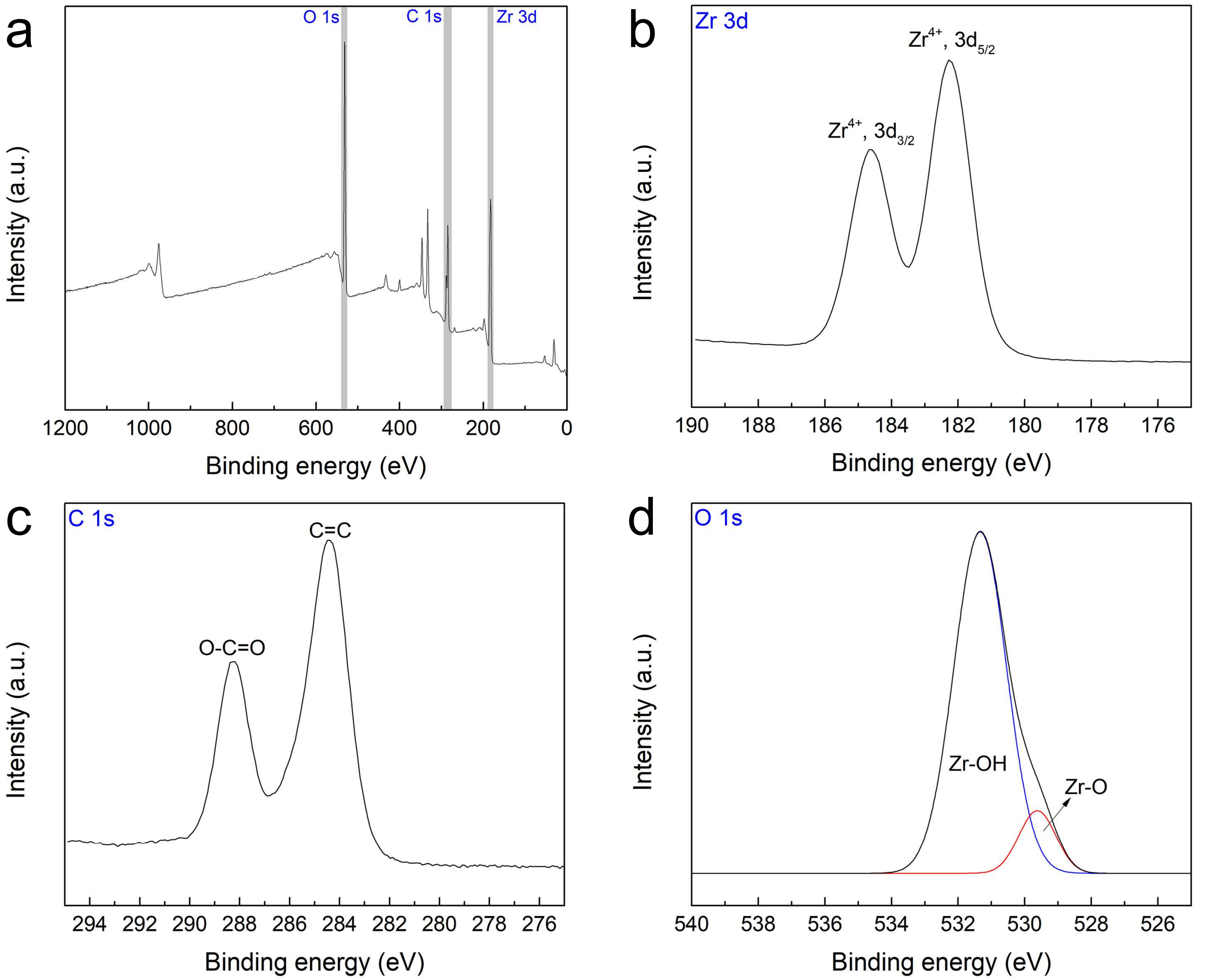

Supplementary Fig. 14. XPS spectrum of amorphous Zr FMA MOF. **a.** Survey spectrum; **b.** Zr 3d; **c.** C 1s; and **d.** O 1s energy ranges.

Zr, C, and O were detected in the flame synthesized amorphous Zr FMA. The Zr ions were in their +4 oxidation state; the C *1s* spectrum mainly showed C=C bonds, as well as a peak for O-C=O bonds from the carboxyl group of Zr FMA; the O *1s* spectrum showed the main zirconium hydroxyl bond and the Zr-O bond. This XPS spectrum was consistent with previously reported crystalline Zr MOF-801.[2]

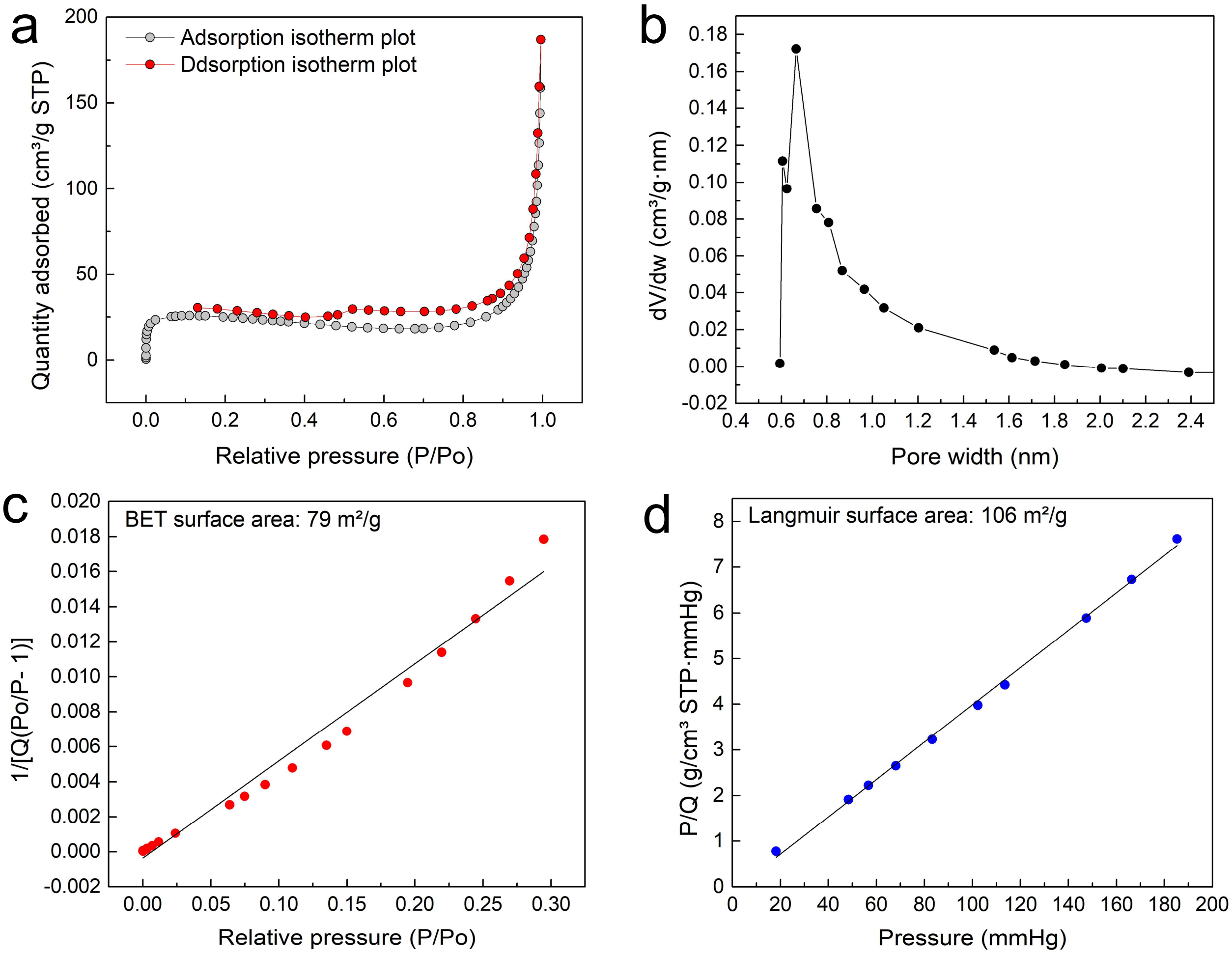

Supplementary Fig. 15. Pore structure analysis of amorphous Zr FMA MOF. **a.** N_2 adsorption/desorption isotherm plots; **b.** Horvath-Kawazoe differential pore volume plot; **c.** BET surface area plot and **d.** Langmuir surface area plot.

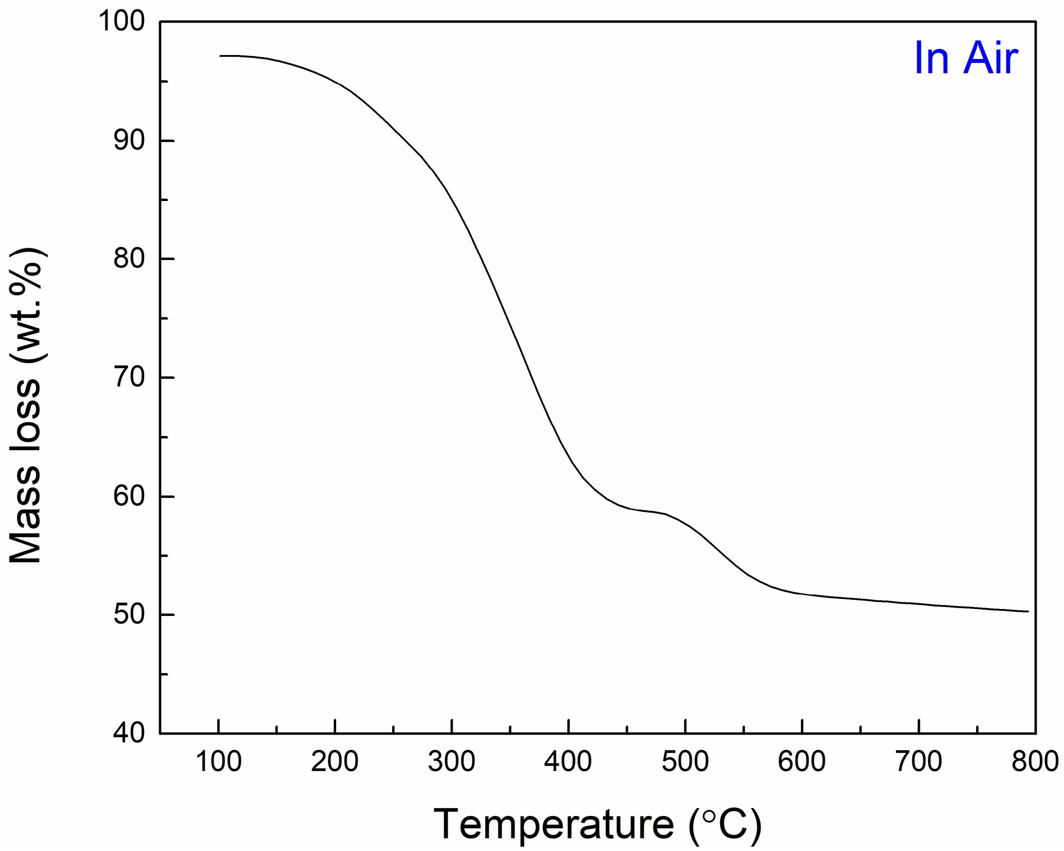

Supplementary Fig. 16. TGA analysis of amorphous Zr FMA MOF in air.

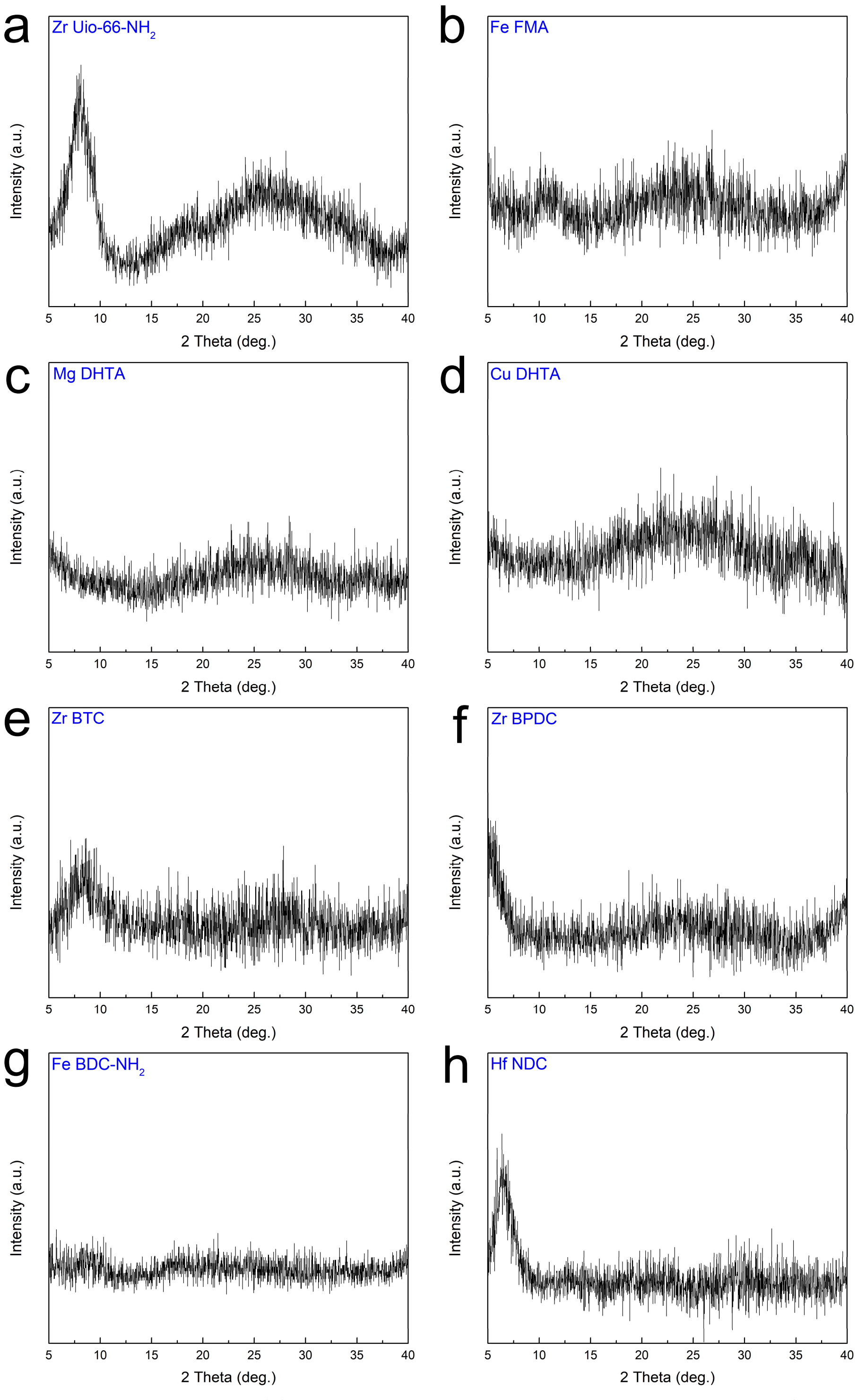

Supplementary Fig. 17. Library of flame aerosol synthesized amorphous MOFs. XRD patterns of **a.** Zr UiO-66-NH$_2$; **b.** Fe FMA; **c.** Mg DHTA; **d.** Cu DHTA; **e.** Zr BTC; **f.** Zr BPDC; **g.** Fe BDC-NH$_2$ and **h.** Hf NDC.

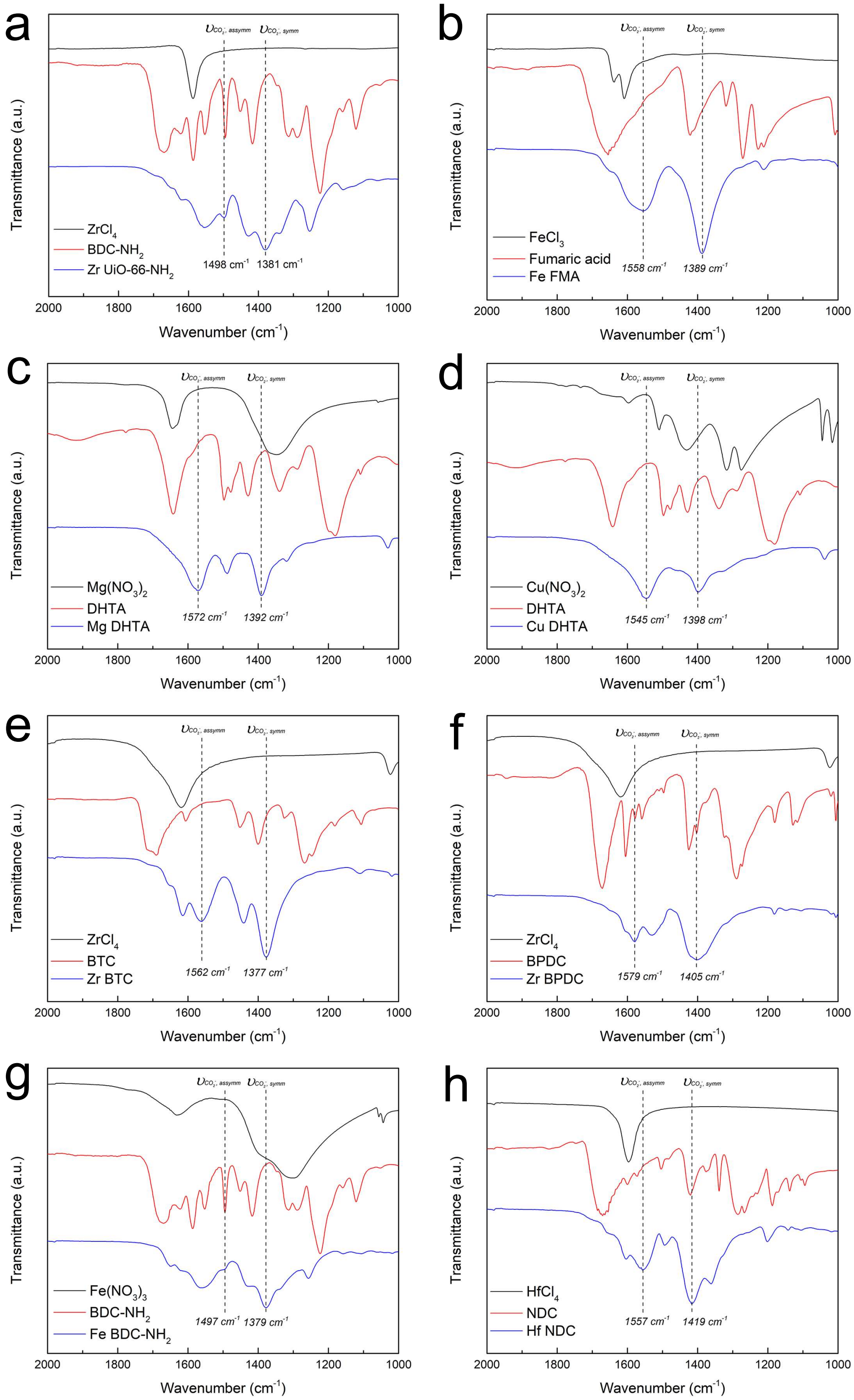

Supplementary Fig. 18. FTIR spectra of amorphous MOFs **a.** Zr UiO-66-NH_2; **b.** Fe FMA; **c.** Mg DHTA; **d.** Cu DHTA; **e.** Zr BTC; **f.** Zr BPDC; **g.** Fe BDC-NH_2 and **h.** Hf NDC, as well as their reactants.

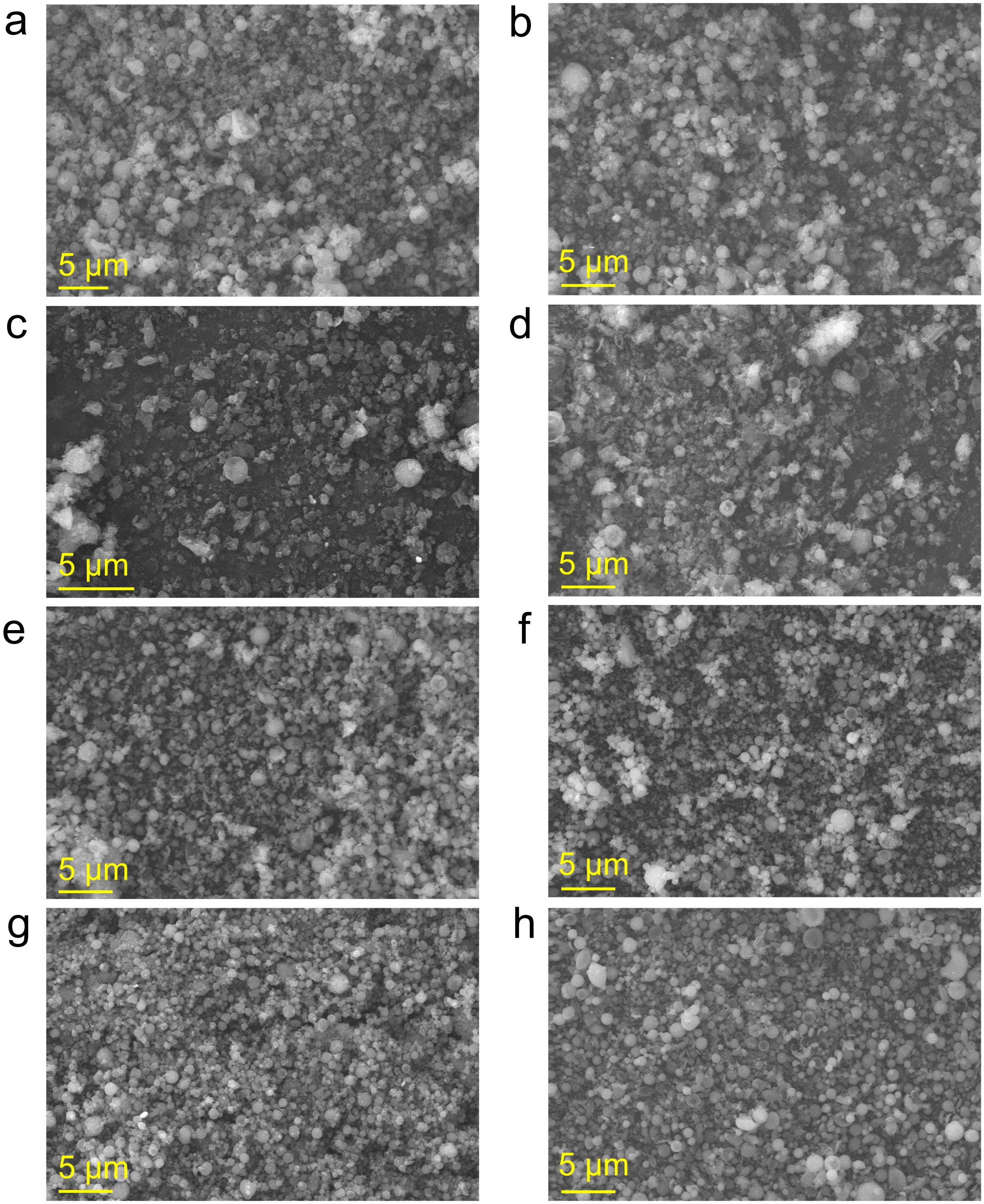

Supplementary Fig. 19. Representative SEM images of flame aerosol synthesized amorphous MOFs. **a.** Zr UiO-66-NH_2; **b.** Fe FMA; **c.** Mg DHTA; **d.** Cu DHTA; **e.** Zr BTC; **f.** Zr BPDC; **g.** Fe BDC-NH_2 and **h.** Hf NDC.

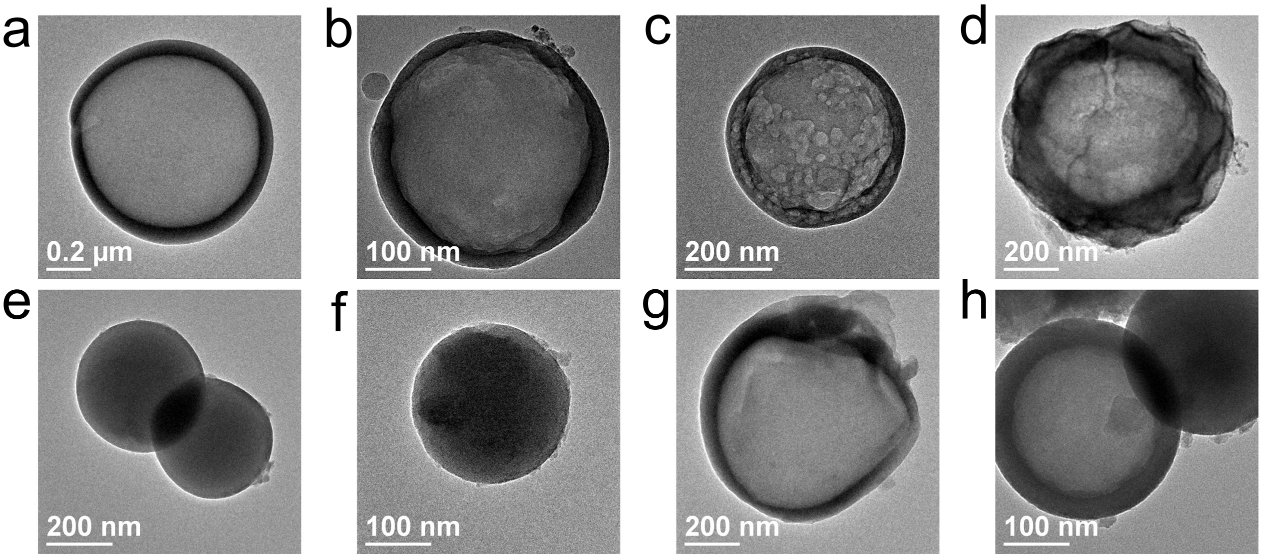

Supplementary Fig. 20. Representative TEM images of flame aerosol synthesized amorphous MOFs. **a.** Zr UiO-66-NH_2; **b.** Fe FMA; **c.** Mg DHTA; **d.** Cu DHTA; **e.** Zr BTC; **f.** Zr BPDC; **g.** Fe BDC-NH_2 and **h.** Hf NDC.

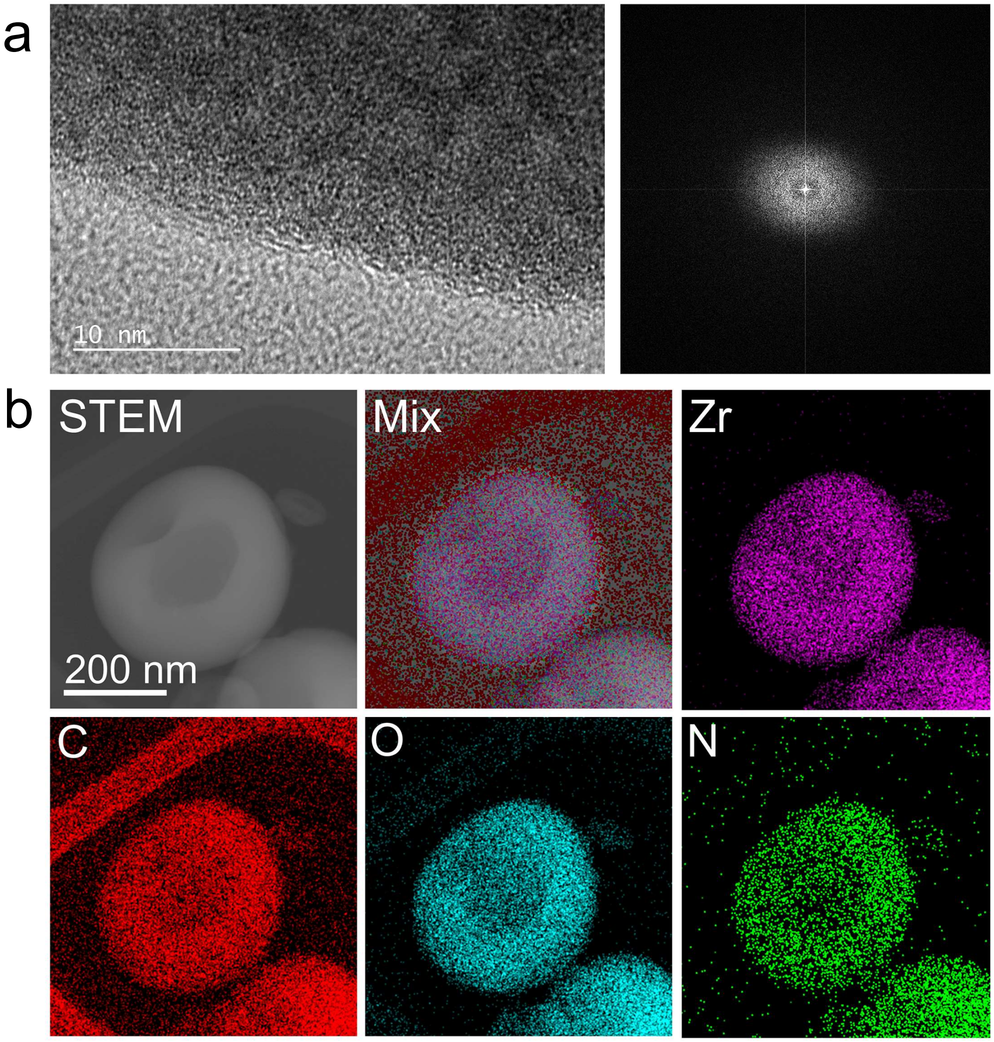

Supplementary Fig. 21. a. HRTEM image and corresponding FFT and **b.** HAADF-STEM EDS maps of amorphous Zr UiO-66-NH_2 MOF.

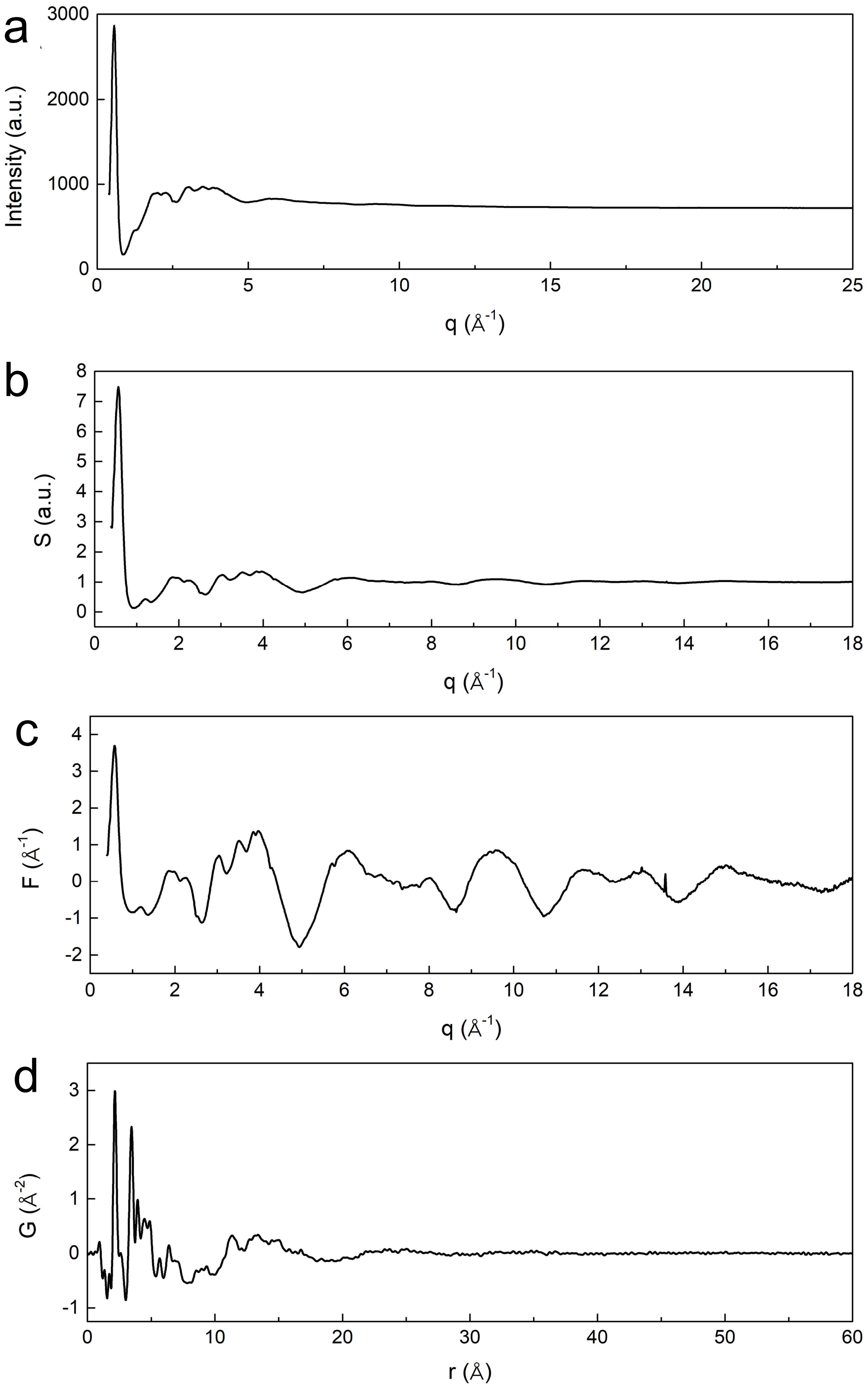

Supplementary Fig. 22. a. X-ray total scattering pattern; **b.** Static structure factor; **c.** Fourier transform function of S (Q) and **d.** Pair distribution function (PDF) of amorphous Zr UiO-66-NH_2 MOF.

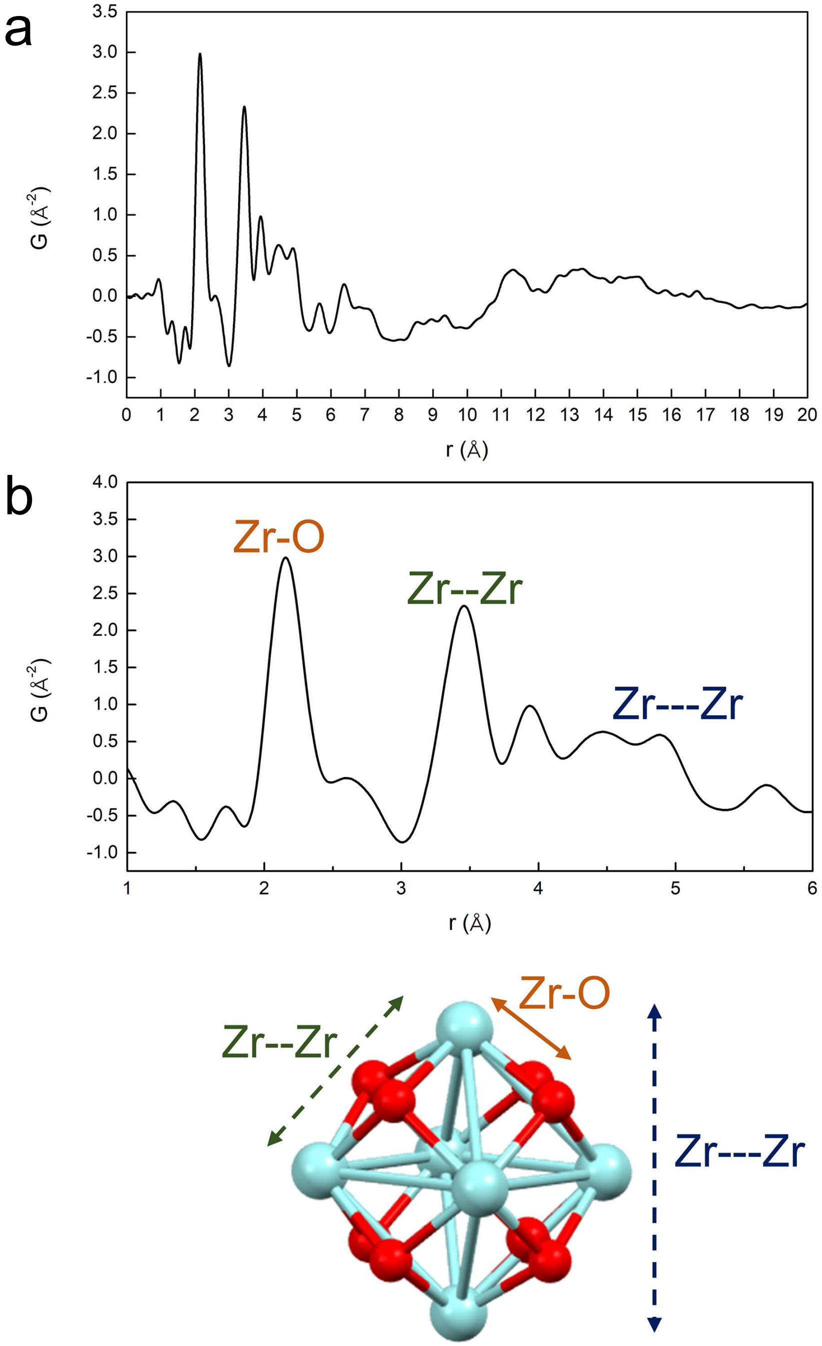

Supplementary Fig. 23. Zoomed-in PDF patterns of the Zr UiO-66-NH_2 MOF in the **a.** 0–20 Å and **b.** 0–6 Å regions. The blue atom is Zr and red atom is O.

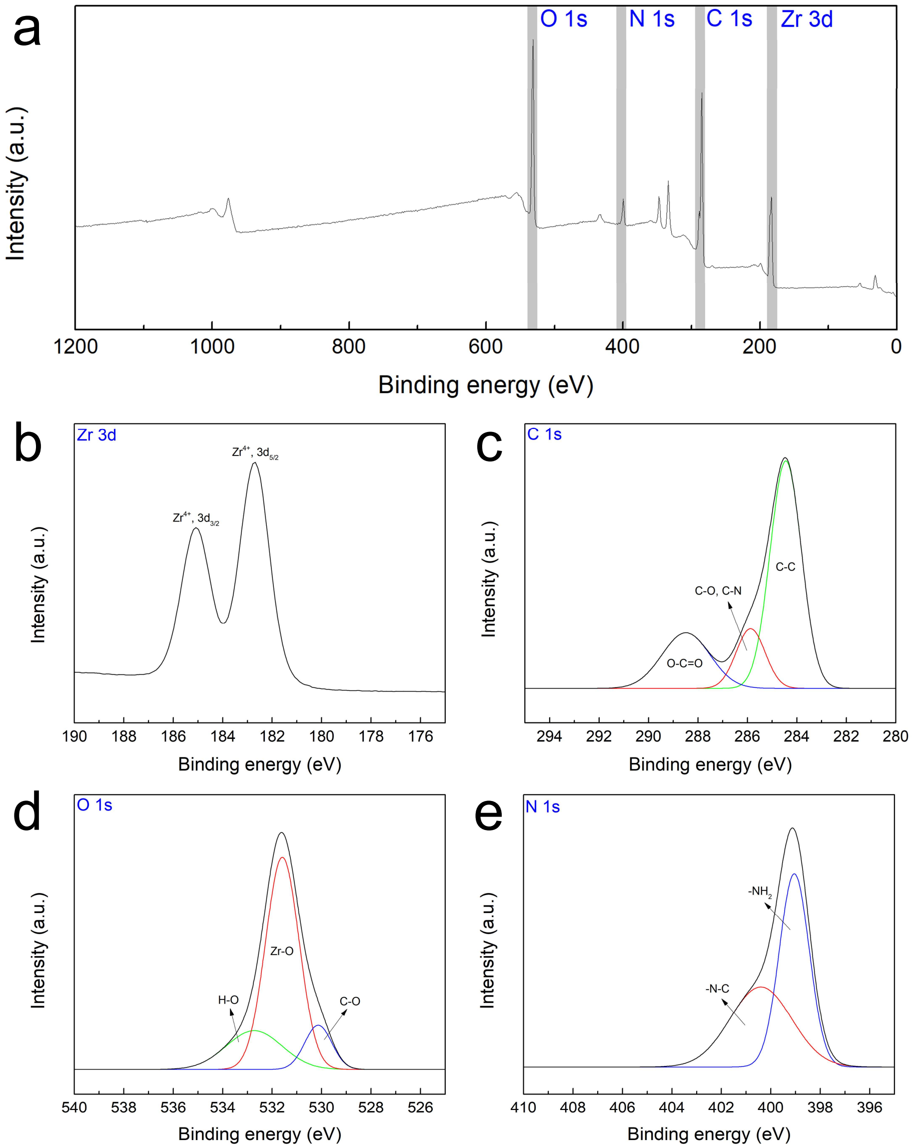

Supplementary Fig. 24. XPS spectrum of amorphous Zr UiO-66-NH_2 MOF. **a.** Survey spectrum; **b.** Zr 3d; **c.** C 1s; **d.** O 1s and **e.** N 1s energy ranges.

Zr, C, O, and N were detected in the flame synthesized amorphous UiO-66-NH_2 MOF. The Zr ions were in a +4 oxidation state; the C *1s* spectrum mainly showed C-C bonds, but peaks for O-C=O, C-O, and C-N were also detected; the O *1s* spectrum showed the Zr-O bond, C-O bond, and surface adsorbed H_2O; the N *1s* spectrum corresponded to $-NH_2$ and N−C. This XPS spectrum was consistent with previously reported crystalline UiO-66-NH_2.[3]

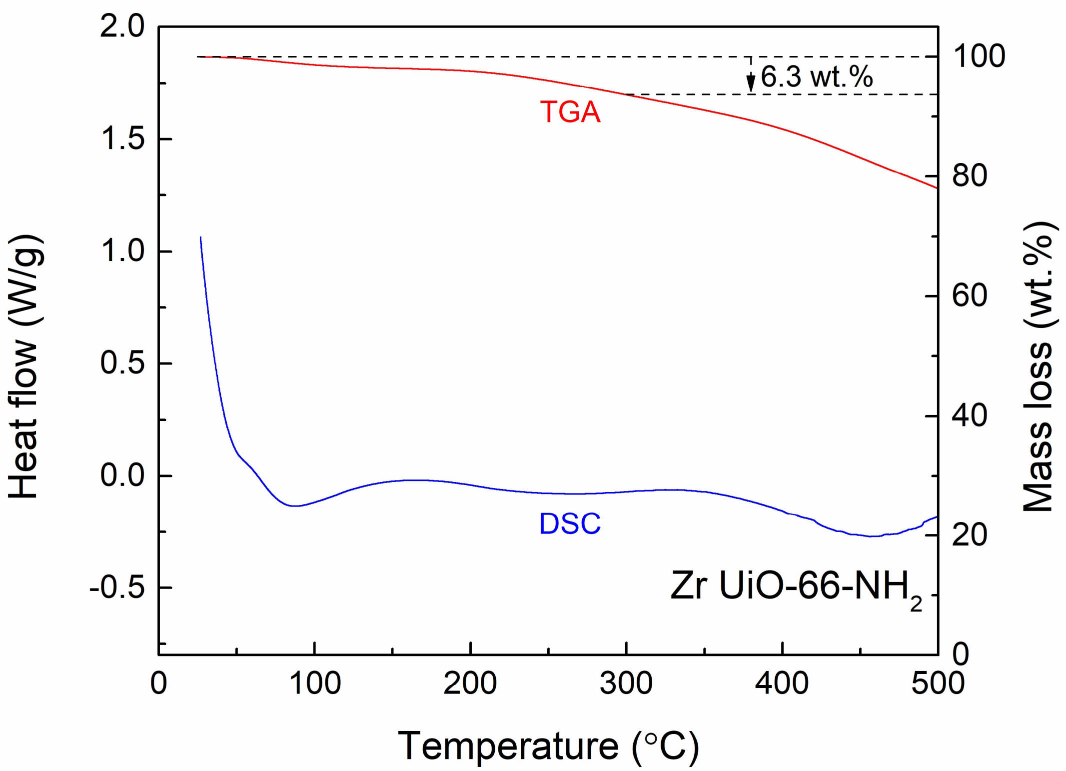

Supplementary Fig. 25. DSC-TGA analysis of amorphous Zr UiO-66-NH$_2$ MOF.

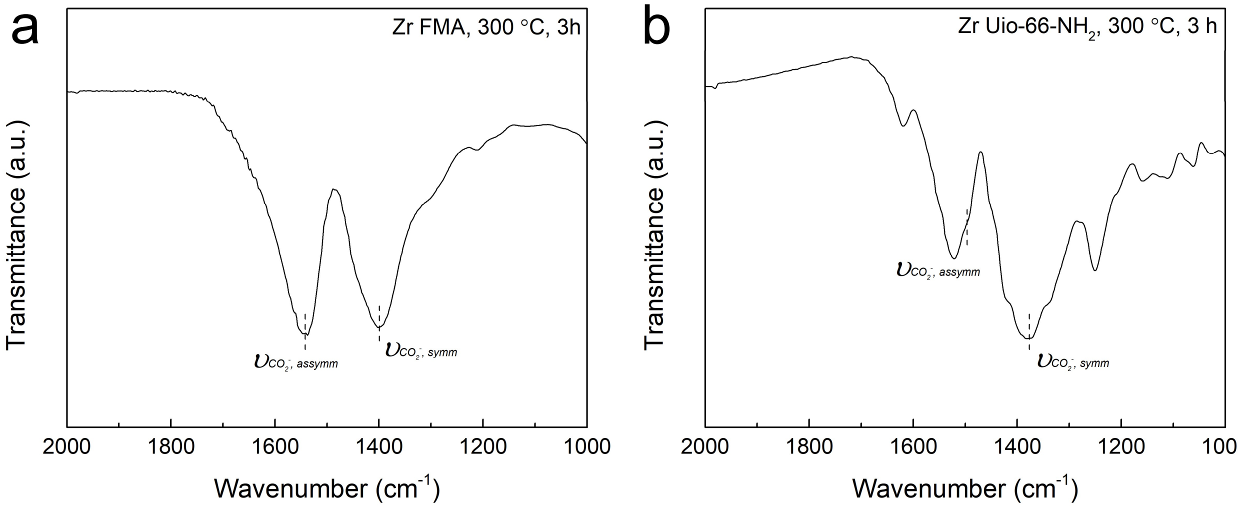

Supplementary Fig. 26. FTIR spectra of amorphous **a.** Zr FMA and **b.** Zr UiO-66-NH$_2$ MOFs heated in Ar at 300 ºC for 3 hours.

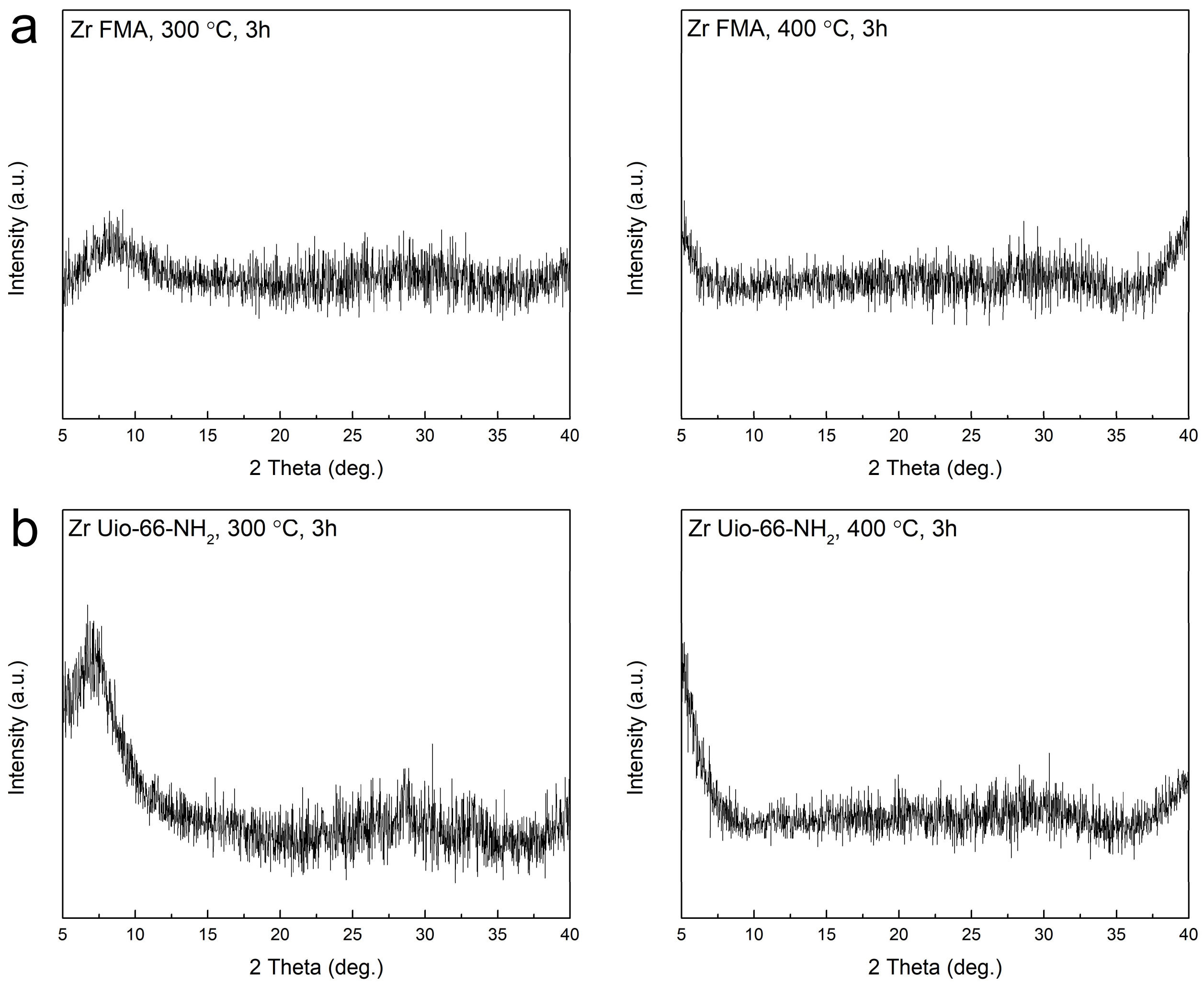

Supplementary Fig. 27. XRD patterns of amorphous **a.** Zr FMA and **b.** Zr UiO-66-NH_2 heated in Ar at 300 ºC and 400 ºC for 3 hours.

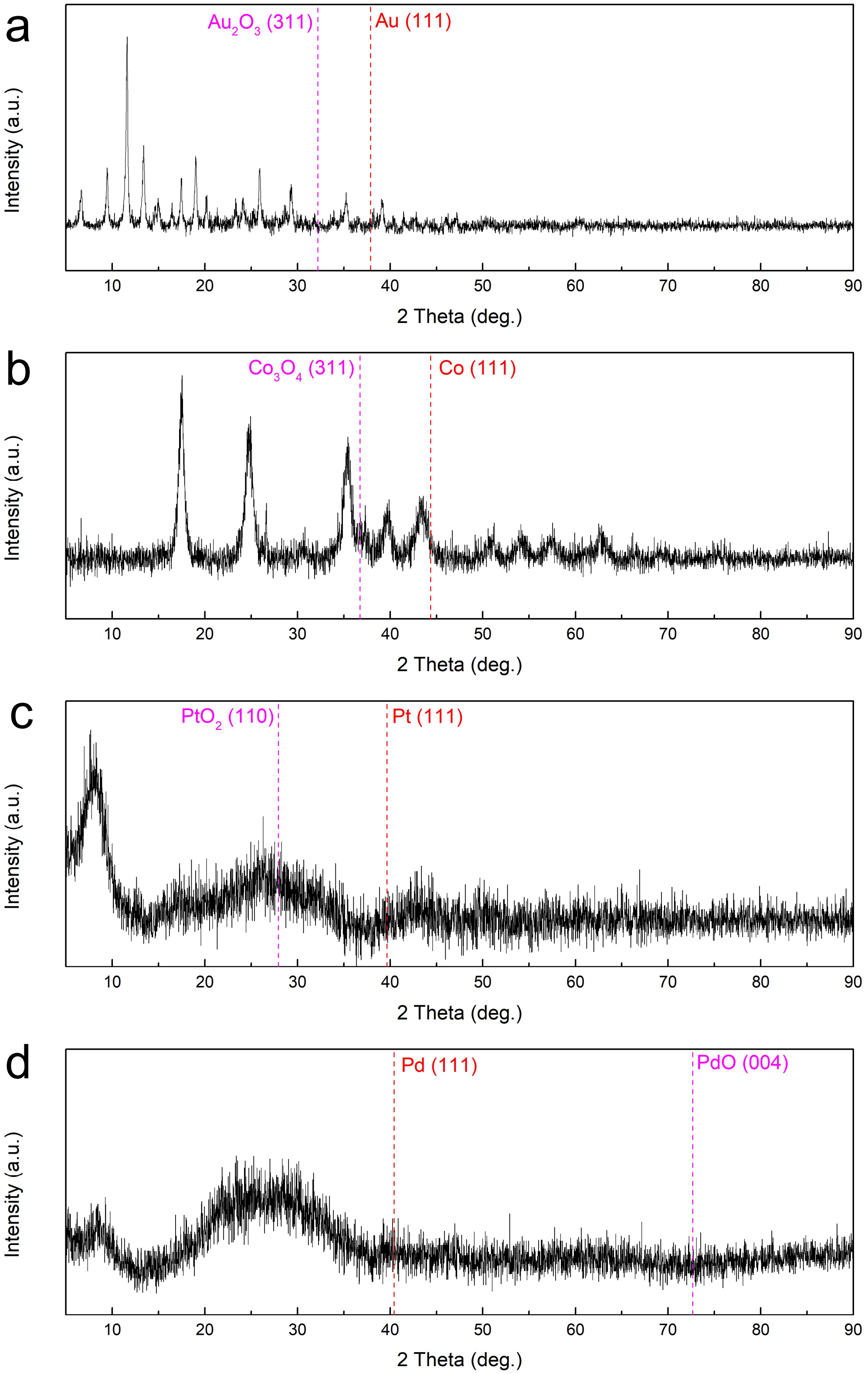

Supplementary Fig. 28. XRD patterns of **a.** single atom Au in Cu HKUST-1; **b.** single atom Co in Ni PBA; **c.** single atom Pt in amorphous Zr UiO-66-NH_2 and **d.** single atom Pd in amorphous Zr FMA.

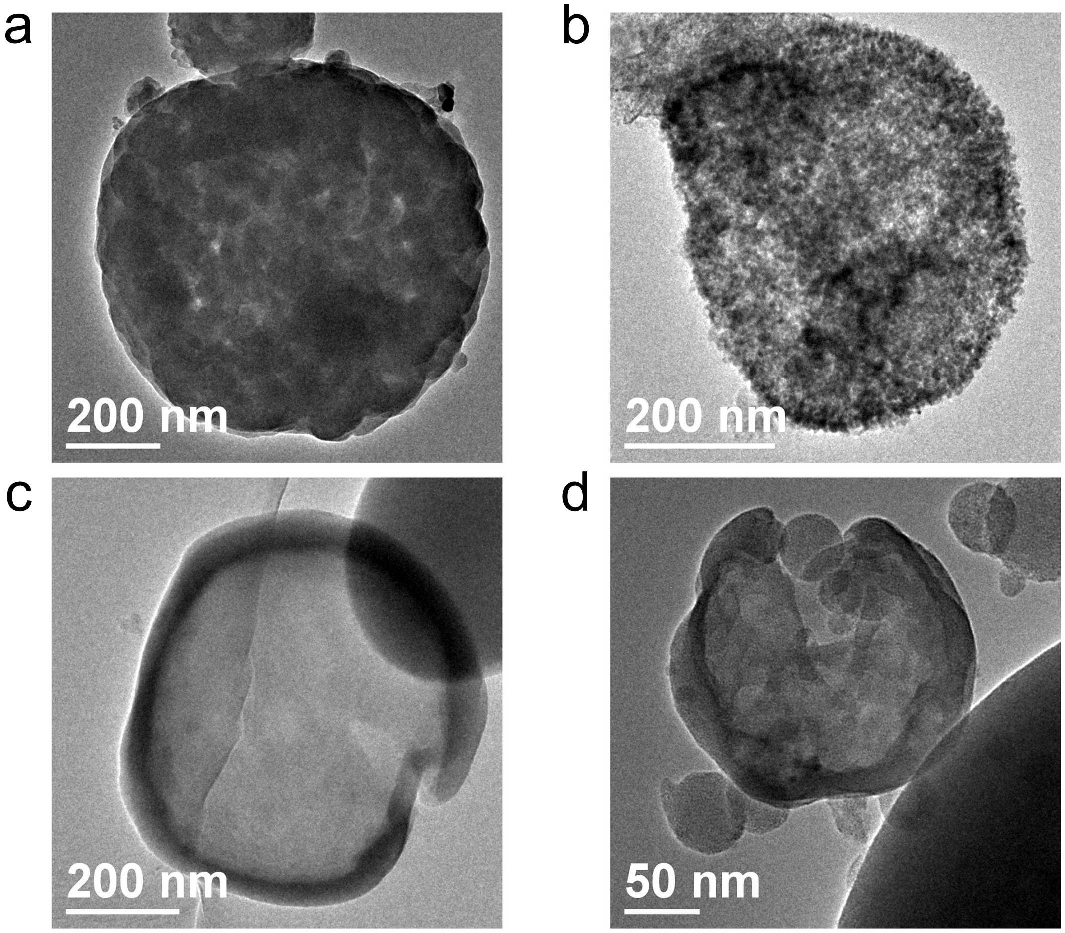

Supplementary Fig. 29. TEM images of **a.** single atom Au in Cu HKUST-1; **b.** single atom Co in Ni PBA; **c.** single atom Pt in amorphous Zr UiO-66-NH_2 and **d.** single atom Pd in amorphous Zr FMA.

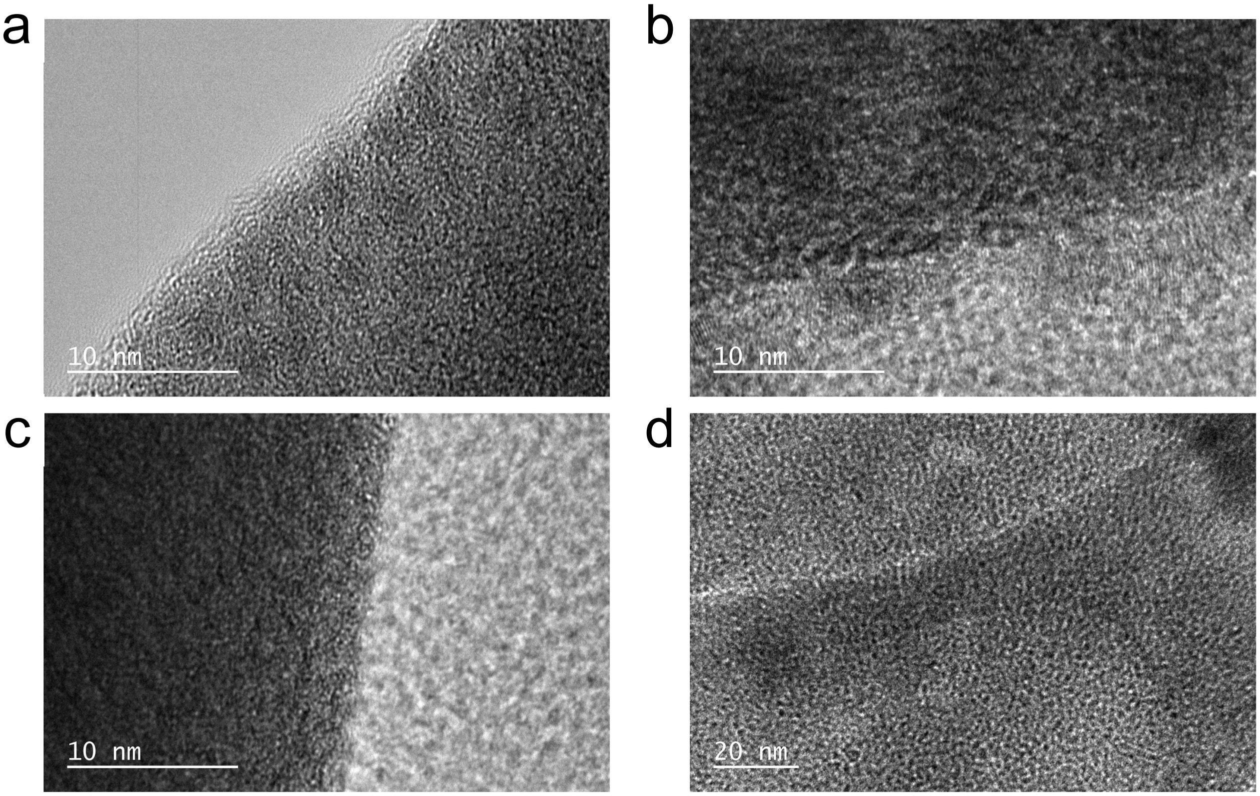

Supplementary Fig. 30. HRTEM images of **a.** single atom Au in Cu HKUST-1; **b.** single atom Co in Ni PBA; **c.** single atom Pt in amorphous Zr UiO-66-NH$_2$ and **d.** single atom Pd in amorphous Zr FMA.

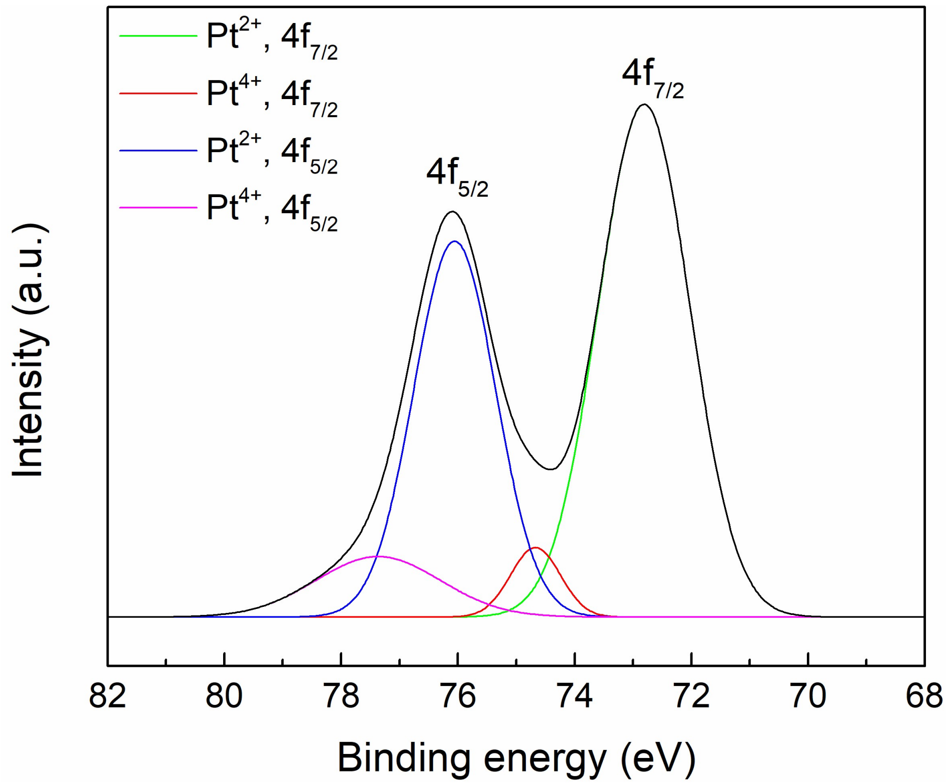

Supplementary Fig. 31. Pt *4f* XPS spectrum of single atom Pt in amorphous Zr UiO-66-NH$_2$.

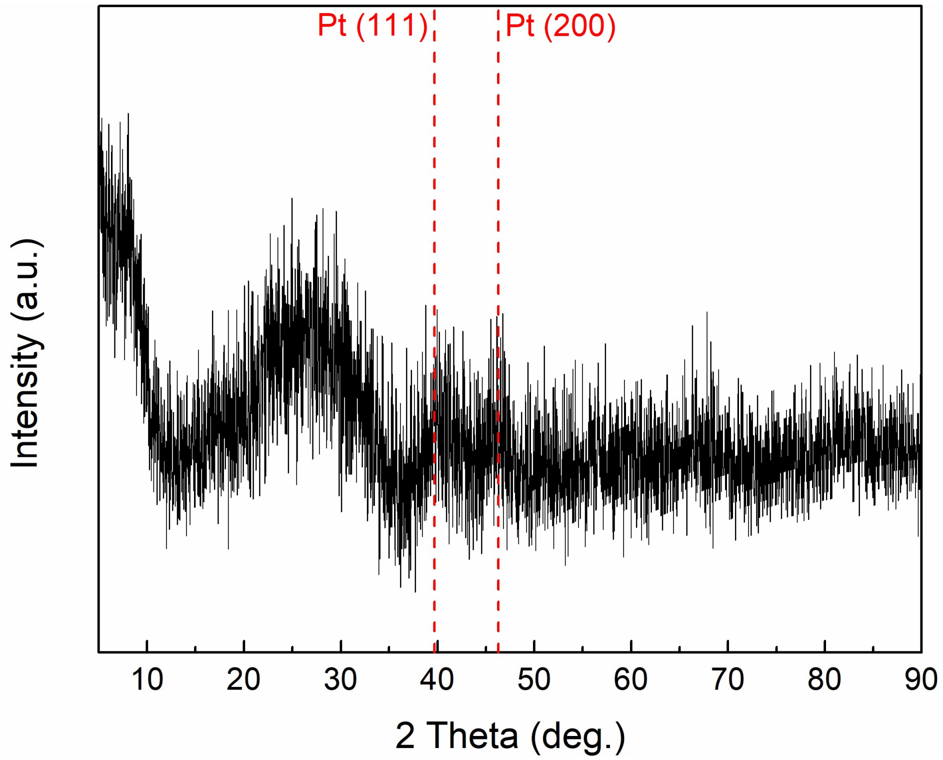

Supplementary Fig. 32. XRD pattern of Pt nanoclusters on Zr UiO-66-NH_2 amorphous MOF after reduction.

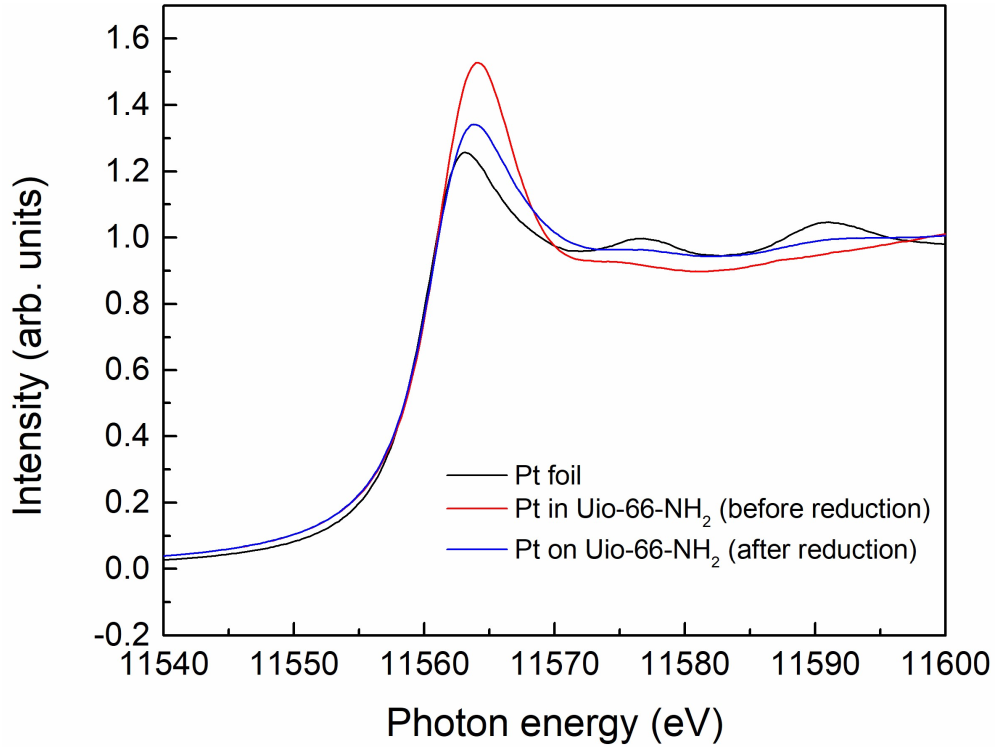

Supplementary Fig. 33. XANES spectra at the Pt L_3-*edge* of Pt foil, single atom Pt in Zr UiO-66-NH$_2$ and Pt nanoclusters on Zr UiO-66-NH$_2$ amorphous MOF.

Pt L_3-*edge* X-ray absorption near edge structure (XANES) spectra recorded for the studied materials, as well as Pt foil as reference. The intensive edge feature, often referred to as white-line (WL), originates from $2p_{3/2} \rightarrow 5d$ electron transition. The intensity of the white-line is strongly correlated with the oxidation state, where higher occupancy of the 5d state results in less intense WL. The intensity of the WL in the XANES spectra suggests that Pt species before reduction are exclusively in oxidized form, while for the material after reduction a significant fraction of Pt is present in metallic form. The lack of long-range order suggests higher dispersion degree compared to Pt foil.

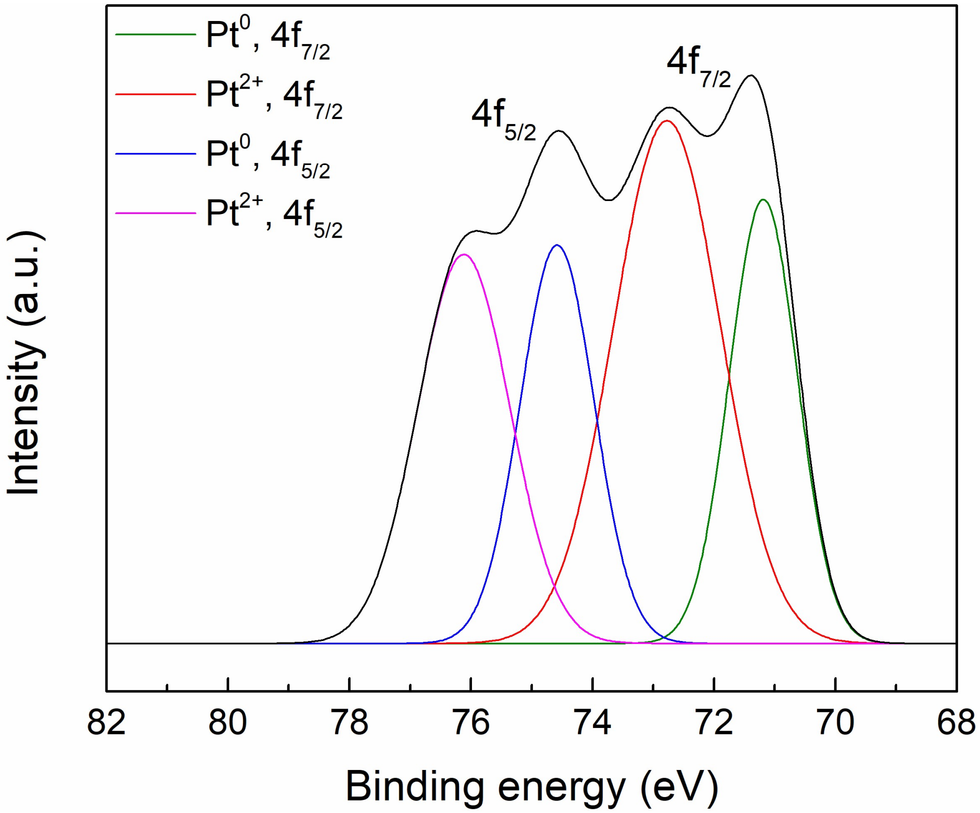

Supplementary Fig. 34. Pt *4f* XPS spectrum of Pt nanoclusters on Zr UiO-66-NH_2 amorphous MOF after reduction.

We attribute the detected Pt^{2+} species to surface oxidation of Pt nanoparticles in air.

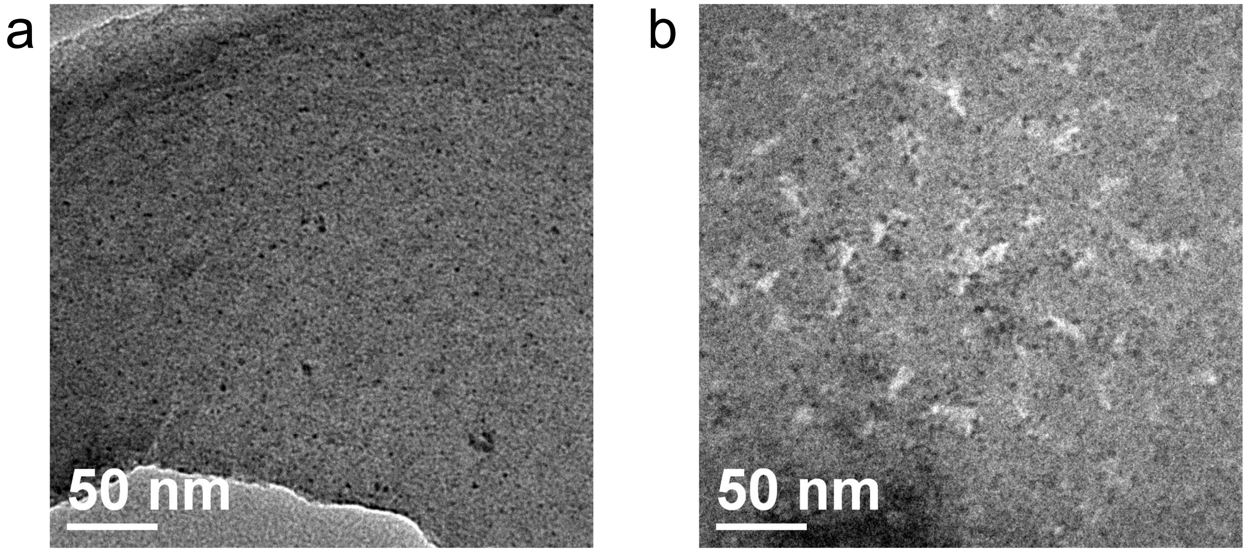

Supplementary Fig. 35. TEM images of Pd nanoclusters on amorphous **a.** Zr UiO-66-NH_2 and **b.** Zr FMA MOFs, fabricated by $NaBH_4$ reduction of single atom Pd in Zr UiO-66-NH_2 and Zr FMA.

Supplementary Tables

Supplementary Table 1. Precursor solution compositions used for preparing crystalline MOFs

MOF	Metal	Ligand	Metal concentration (mM)	Metal:ligand (mol.%)	Solvent
Cu HKUST-1	$Cu(NO_3)_2 \cdot 3H_2O$	1,3,5-Benzenetricarboxylic acid	20~60	3:2	DMF:EtOH:H_2O=1:1:3
Cu BDC	$Cu(NO_3)_2 \cdot 3H_2O$	1,4-Benzenedicarboxylic acid	20	1:1	DMF:H_2O=2:3
Tb PDA	$Tb(NO_3)_2 \cdot 6H_2O$	1,4-Phenylenediacetic acid	14	7:11	DMF:H_2O=2:3
Cu FMA	$Cu(NO_3)_2 \cdot 3H_2O$	Fumaric acid	30	1:1	DMF:EtOH:H_2O=1:1:3
Ni PBA	$Ni(NO_3)_2 \cdot 6H_2O$	N.A.	40	2:1	H_2O
	N.A.	Potassium ferricyanide	20		H_2O
Zn BDC-NH_2	$Zn(NO_3)_2 \cdot 6H_2O$	2-Aminobenzene-1,4-dicarboxylic acid	20	2:1	DMF:EtOH:H_2O=1:1:3
Zn BTC	$Zn(NO_3)_2 \cdot 6H_2O$	1,3,5-Benzenetricarboxylic acid	30	3:2	DMF:EtOH:H_2O=1:1:3
Cu PMA	$Cu(NO_3)_2 \cdot 3H_2O$	Pyromellitic acid	30	3:2	DMF:EtOH:H_2O=1:1:3
Cu BTB	$Cu(NO_3)_2 \cdot 3H_2O$	1,3,5-Tris(4-carboxyphenyl) benzene	21	3:2	DMF:EtOH:H_2O=1:1:3

Note: For Ni PBA, the metal and ligand precursors are contained in different flasks and injected into the reactor at the same time.

Supplementary Table 2. Precursor solution compositions used for synthesis of amorphous MOFs

MOF	Metal	Ligand	Metal concentration (mM)	Metal:ligand (mol.%)	Solvent
Zr FMA	$ZrOCl_2•8H_2O$	Fumaric acid	20	1:1	DMF:Formic acid:H_2O=4:1:6
Zr UiO-66-NH_2	$ZrCl_4$	2-Aminobenzene-1,4-dicarboxylic acid	20	1:1	DMF:H_2O=2:3
Fe FMA	$FeCl_2•4H_2O$	Fumaric acid	30	1:1	DMF:H_2O=2:3
Mg DHTA	$Mg(NO_3)_2•6H_2O$	2,5-Dihydroxyterephthalic acid	30	3:1	DMF:H_2O=2:3
Cu DHTA	$Cu(NO_3)_2•3H_2O$	2,5-Dihydroxyterephthalic acid	20	2:1	DMF:H_2O=2:3
Zr BTC	$ZrCl_4$	1,3,5-Benzenetricarboxylic acid	20	3:1	DMF:EtOH:H_2O=1:1:3
Zr BPDC	$ZrCl_4$	Biphenyl-4,4′-dicarboxylic acid	20	10:7	DMF:H_2O=2:3
Fe BDC-NH_2	$Fe(NO_3)_2•9H_2O$	2-Aminobenzene-1,4-dicarboxylic acid	30	2:1	DMF:EtOH:H_2O=1:1:3
Hf NDC	$HfCl_4$	N.A.	40	1:1	DMF:H_2O=2:3
	N.A.	2,6-Naphthalenedicarboxylic acid	40		DMF:H_2O=2:3

Note: For Hf NDC, the metal and ligand precursors are contained in different flasks and injected into the reactor at the same time.

Supplementary Table 3. Microporous structure analysis of flame synthesized Cu-HKUST using different Cu concentrations in precursor solution

Cu concentration (mM)	BET surface area (m^2/g)	Langmuir surface area (m^2/g)	Pore volume (cm^3/g)	Median pore width (Å)
20	818	1414	0.390	4.46
40	1024	1680	0.517	4.51
60	1052	1707	0.522	4.51

Note: The pore volume and median pore width are calculated by the Horvath-Kawazoe method.

Supplementary Table 4. Refined XRD peak information of flame synthesized Cu KHUST-1

No.	2-theta (deg)	d (Å)	Height (cps)	FWHM (deg)	Size (Å)
1	6.03	14.64	116.41	0.30	279
2	6.91	12.79	375.08	0.28	292
3	9.72	9.09	350.04	0.29	284
4	11.85	7.46	1225.97	0.25	334
5	13.62	6.50	187.34	0.26	316
6	14.83	5.97	153.51	0.34	247
7	16.67	5.31	94.83	0.30	283
8	17.68	5.01	263.24	0.26	319
9	19.25	4.61	319.37	0.25	337
10	20.42	4.36	132.05	0.31	274
11	21.50	4.13	41.81	0.29	288
12	23.54	3.78	19.65	0.29	289
13	24.36	3.65	84.53	0.57	150
14	26.19	3.40	164.94	0.26	299
15	27.92	3.20	44.92	0.55	155
16	28.92	3.08	50.28	0.26	334
17	29.58	3.02	151.75	0.29	294
18	31.12	2.87	23.27	0.29	294
19	31.98	2.80	34.25	0.29	296
20	35.45	2.53	118.07	0.37	238
21	38.15	2.36	33.84	0.29	300
22	39.35	2.29	114.02	0.34	259

Supplementary Table 5. Refined XRD peak information of the Cu BDC

No.	2-theta (deg)	d (Å)	Height (cps)	FWHM (deg)	Size (Å)
1	8.40	10.52	490.11	0.32	259
2	15.37	5.76	110.18	0.34	243
3	16.71	5.30	219.76	0.29	291
4	25.09	3.55	44.45	0.60	142
5	26.40	3.37	111.02	1.42	60
6	29.79	3.00	50.45	2.29	38
7	31.11	2.87	27.91	0.60	144
8	33.90	2.64	54.24	0.60	145
9	34.54	2.59	23.9	0.60	145

Supplementary Table 6. Refined XRD peak information of the Tb PDA

No.	2-theta (deg)	d (Å)	Height (cps)	FWHM (deg)	Size (Å)
1	8.30	10.64	63.52	0.30	274
2	9.59	9.22	56.95	0.29	289
3	11.35	7.79	31.31	0.46	180
4	16.38	5.41	31.63	0.56	151

Supplementary Table 7. Refined XRD peak information of the Cu FMA

No.	2-theta (deg)	d (Å)	Height (cps)	FWHM (deg)	Size (Å)
1	10.25	8.62	650.92	0.36	231
2	10.78	8.20	384.67	0.39	212
3	14.76	6.00	105.09	0.84	100
4	17.81	4.98	27.43	0.45	186
5	18.79	4.72	17.36	0.45	186
6	20.51	4.33	200.37	0.39	216
7	21.65	4.10	36.19	0.45	187
8	22.43	3.96	48.34	4.94	17
9	22.78	3.90	35.97	0.45	187
10	30.98	2.88	167.55	0.45	190

Supplementary Table 8. Refined XRD peak information of the Ni PBA

No.	2-theta (deg)	d (Å)	Height (cps)	FWHM (deg)	Size (Å)
1	17.61	5.03	63.15	0.86	98
2	24.85	3.58	51.43	1.07	79
3	35.42	2.53	58.68	1.01	86
4	37.40	2.40	5.78	1.01	87
5	39.74	2.267	6.42	1.01	87

Supplementary Table 9. Refined XRD peak information of the Zn BDC-NH_2

No.	2-theta (deg)	d (Å)	Height (cps)	FWHM (deg)	Size (Å)
1	6.77	13.04	26.84	1.12	74
2	9.77	9.05	324.58	0.31	267
3	13.83	6.40	89.76	0.26	282
4	15.44	5.74	16.07	1.12	75
5	20.60	4.31	21.53	1.12	75
6	22.74	3.91	21.82	1.12	75
7	31.79	2.81	17.77	1.12	77

Supplementary Table 10. Refined XRD peak information of the Zn BTC

No.	2-theta (deg)	d (Å)	Height (cps)	FWHM (deg)	Size (Å)
1	10.36	8.53	141.88	0.96	87
2	11.82	7.48	36.44	0.65	128

Supplementary Table 11. Refined XRD peak information of the Cu PMA

No.	2-theta (deg)	d (Å)	Height (cps)	FWHM (deg)	Size (Å)
1	10.83	8.16	447.5	0.22	385
2	15.39	5.75	46.05	0.32	258
3	17.56	5.05	325.41	0.25	337
4	20.06	4.42	167.88	0.47	178
5	24.87	3.58	129.49	0.28	308
6	26.70	3.33	129.84	0.62	137
7	33.37	2.68	42.53	0.32	267
8	35.62	2.52	54.54	0.52	167

Supplementary Table 12. Refined XRD peak information of the Cu BTB

No.	2-theta (deg)	d (Å)	Height (cps)	FWHM (deg)	Size (Å)
1	6.05	14.58	108.77	1.38	60
2	10.92	8.10	23.41	1.03	81

Supplementary Table 13. ICP analysis of the doped metals in MOFs

Bi-metallic MOFs	Designed in precursor (M_1:(M_1+M_2) in mol.)	ICP measured in product (M_1:(M_1+M_2) in mol.)
Au-Cu HKUST-1	0.050	0.026
Co-Ni PBA	0.100	0.106
Pt-Zr UiO-66-NH_2	0.100	0.074
Pd-Zr FMA	0.100	0.081

Supplementary Table 14. EXAFS best fitting parameters for the studied materials

Material	Path	CN	R (Å)	σ^2 (Å^2)	ΔE
Pt in UiO-66-NH$_2$ (Before reduction)	Pt-O	1.9 +/- 0.6	1.90 +/- 0.01	0.006	-9.3
	Pt-O	9.7 +/- 0.5	2.41 +/- 0.03	0.009	
Pt on UiO-66-NH$_2$ (After reduction)	Pt-Pt	2.5 +/- 0.7	2.72 +/- 0.02	0.004	4.5

For the material before reduction, the first shell peak between 1.91 Å arises from Pt-O scattering, and the EXAFS fitting results suggest a first shell coordination number of 1.9 for the Pt. Second scattering peak arises from an oxygen shell further away from the Pt site with a bond distance of 2.41 Å, and coordination number of 9.7. Additionally, for the material after reduction, a 3rd shell could be fitted arising from Pt-Pt scattering at 2.72 Å with a coordination number of 2.5.

Supplementary References

1. Han, S., Ciufo, R.A., Meyerson, M.L., Keitz, B.K. & Mullins, C.B. Solvent-free vacuum growth of oriented HKUST-1 thin films. *J. Mater. Chem. A* **7**, 19396-19406 (2019).
2. Zhu, X.-H., Yang, C.-X. & Yan, X.-P. Metal-organic framework-801 for efficient removal of fluoride from water. *Microporous Mesoporous Mat.* **259**, 163-170 (2018).
3. Liu, J. et al. NH(3) Plasma Functionalization of UiO-66-NH_2 for Highly Enhanced Selective Fluorescence Detection of U(VI) in Water. *Anal. Chem.* **94**, 10091-10100 (2022).